Scientific Research Publishing

Advances in Aerospace Science and Technology, 2025, 10(4), 135-172
https://www.scirp.org/journal/aast
ISSN Online: 2473-6724
ISSN Print: 2473-6708

Optimizing Computational Efficiency with Preliminary 2D CFD for Ground-Effect Flight Transit Vehicle Design

Adam B. Suppes, Galen J. Suppes

HS-Drone, LLC, Charlottesville, USA
Email: suppesadam@gmail.com

How to cite this paper: Suppes, A.B. and Suppes, G.J. (2025) Optimizing Computational Efficiency with Preliminary 2D CFD for Ground-Effect Flight Transit Vehicle Design. *Advances in Aerospace Science and Technology*, **10**, 135-172.
https://doi.org/10.4236/aast.2025.104010

Received: October 23, 2025
Accepted: November 29, 2025
Published: December 2, 2025

Abstract

Early stages of ground-effect flight transit vehicle (GEFT) development identify benchmark digital prototype performances with approaches to reduce energy consumption by 20% to 80%. 80% reductions are possible when aerodynamic suspension mitigates rolling losses. Applications range from reducing drag for automobiles to railcars operating in ground-effect flight at greater speeds on existing track infrastructure. The technology utilizes a trailing-section upper-surface ducted fan, a trailing tapered surface, and a lower cavity comprising side fences and a trailing flap. These additional features both enable higher levels of performance and increase the degrees of freedom for computational optimization. This paper uses a minimum in total Computational Fluid Dynamics (CFD) mesh turbulence as a method to identify the local optimal ducted fan power setting and to compare different designs. Three-dimensional simulations identified a range of viable design applications for constant airfoil cross sections. Applications are limited by the vehicles' ratios of thickness to length (thickness ratio) and the ratios of width to length (aspect ratio). Analysis is limited to vehicles 2.6 m wide for compatibility with multimodal operation on existing highway and railway corridors. The work creates the opportunity to test the limits of modern computational methods to rapidly advance designs through the application of extrapolating 2D CFD performances to 3D designs and understanding how air flow transforms into lift pressures.

Keywords

Lift, Drag, Computational Fluid Dynamics, Energy Analysis, L/D Efficiency

1. Introduction

This Strategic placement of distributed propulsion on the trailing-section upper-

surface of lifting-body ground-effect vehicles (LB-GEV) can simultaneously reduce drag and rolling losses for a range of wheeled vehicles. Twenty to 80% reductions in energy consumption are attainable with transformative possibilities, dependent on the velocity and application. 20% efficiencies begin at low velocities for automobile applications, while near 80% efficiencies appear at high velocities for trucking applications. However, the multivariable objective-driven optimization includes the addition of ducted fan location, power, and shape as additional degrees of freedom in the already challenging optimization space of the aircraft design.

An efficient approach to this computer-based fluids problem includes use of 2D simulations to screen wing sections for subsequent 3D digital prototype optimizations. The working optimization hypothesis pursues a minimum in turbulence as a metric of minimum lost work and optimal configurations for wing sections coupled with ducted fans. A fundamental based explanation of how air flow generates aerodynamic lift was a valuable supplement to the studies for interpreting 2D simulation results and identifying how to approach 2D performance with 3D digital prototypes. This paper simultaneously evolves the optimization methodology and the vehicle design.

The technology enables open-ended evolution with far greater possibilities than current transit options. The science and technology are enabled by computational fluid dynamics (CFD) for rapid progress, optimization, and evolution.

2. Background

It is possible to both: a) reduce energy consumption by 20% to 80% for a gamut of vehicles from automobiles to trucks and b) transform ground transportation into a unified multimodal network with substantial reductions in transit times. Initial proof-of-concept studies were based on the use of a recently clarified airfoil science to accurately extrapolate designs [1]. Toward the goal of computer-based results-driven optimization of the lifting-body ground-effect flight vehicles (LB-GEV), 2D simulations can be used to screen designs and narrow the range of parameters to be tested by more computationally-intensive simulations of 3D digital prototypes.

2.1. Source-Body Interference

The optimization problem is particularly complex and computationally intensive due to the manner in which the aerodynamics of propulsor (e.g. a ducted fan) and vehicle wing sections are coupled. A propulsor can be simulated as a velocity "Source" which generates momentum in many computational fluid dynamics packages. In practice, the Source may be a propeller, ducted fan, jet engine, or any of a number of nacelles used in aviation.

For a propeller, the thrust force is collected by pressures on the surfaces of the blades and transmitted to the vehicle through the rotating shaft. A duct can increase fan blade efficiency by reducing the formation of vortex-type turbulence

flowing radially around blade tips, however, the duct's aerodynamic drag is only beneficial when one duct prevents vortex-type turbulence for multiple blades [2]-[7]. The inlets and exhaust nozzles of a ducted fan, including jet engine nacelle, impact the overall effective efficiency of the propulsor [8]-[17].

Low pressures may form at the nacelle inlets and higher pressures may form at the nacelle exhaust nozzles which generate thrust, but the induced and viscous drags are typically greater in magnitude than the "induced thrust" produced by inlet and exhaust nozzles.

When a lifting body surface merges with nacelle surfaces, the propulsor performance and lifting body performance become increasingly coupled and indistinguishable. For example, phenomena such as boundary layer separation become coupled to the interaction. Pressure drag on a wing section can nearly double with the onset of boundary layer separation (BLS), with minor variations in aerodynamic flow determining whether or not BLS occurs.

The current work avoids the topic of decoupling Source and wing section interference by evaluating overall lost work. The hypothesis is that a minimum in lost work translates to an overall optimal efficiency.

2.2. Lost Work in LB-GEV

Several forms of lost work through energy dissipation lead to decreased aircraft efficiency, including:

1) Viscous losses, which include a skin friction component, dissipate to waste heat in near proximity to the surfaces expressing the viscous flow,

2) Higher pressures expand to lower pressures through turbulent flow.

3) Higher pressures expand to lower pressures through diffusion or laminar flow in a manner such that the dilution or flow is not recovered.

Ultimately, all unrecovered flow transforms from organized bulk flow (*i.e.* air velocity) to random increased molecular energy (*i.e.* waste heat).

Since pressure expands at the speed of sound, energy stored as pressure will transform into air flow. Surfaces, such as wing section skins, can block expansion and preserve pressure differences over greater distances. In some instances, the air flow can transform back into pressure such as when streamlines of different velocity vectors merge at trailing-edge stagnation regions.

Ground-effect flight is able to achieve higher efficiency for converting air flow into aerodynamic lift because the ground blocks the downward dissipation of pressure [18]-[24]. Fences or rails traversing most of the vertical gap between the LB-GEV's lower surface and the ground can block most of the lateral dissipation of pressure from a lower cavity.

A hypothesis of the present work is that a dominant indicator of minimum lost work is the minimum in turbulent energy. The hypothesis identifies that: a) unrecovered work in the form of pressure is substantially converted to flow with turbulence and b) changes in viscous lost work are relatively small compared to changes in turbulent lost work. The Results of this work will be evaluated in the

Discussion with respect to this hypothesis.

Preliminary studies have identified that the kinematic turbulence (k) reported by many computational software packages exhibits a minimum as a function of Source power, setting the stage for this work [25].

2.3. 2D versus 3D Performances

In aircraft design, 2D simulations are equivalent to simulating a wing or lifting body of infinite lateral width. Practical designs characterize a vehicle's aspect ratio which is a representative ratio of lateral width to chord length.

3D designs allow for variations in airfoil shape along the lateral dimension. Investigation of lateral variations, except fences, is beyond the scope of the present work.

At a constant airfoil cross section, the fundamental difference between 2D and 3D simulations is accounting for the lateral dissipation of pressure energy. This trend is useful for extrapolating 2D results to 3D performance. For LB-GEV, fences of the lower cavity have been identified as effective to the extent that lift pressures of a well-designed lower cavity of a 3D LB-GEV are able to approach the lower-surface lift pressures of 2D simulations [26] [27].

Key additional design parameters of 3D LB-GEV are the vehicle's aspect ratio, the clearance of the fence with the ground, and the clearance of the trailing flap. A good benchmark value for an average lower surface clearance is 10% of the fuselage thickness. The fences and flap clearances with the ground provide beneficial aerodynamics while distancing the fuselage's lower surface from incidental contact with the ground.

Source power setting, size, and location are prominent operating parameters. The discussion includes findings on the impact of Source location and size.

GEFT technology is in a phase of rapidly increasing evolution and understanding based on the efficiency of CFD methods for evaluating new digital prototypes. The purpose of this paper is to convey understanding and performance capabilities, with some risk of error associated with the absence of direct experimental validation, for the presentation and proof of concept of a hypothesis prior to experimental studies. Unlike past CFD works, this work relates results directly to pressure and velocities forces, using these Three Principles for reference [1]:

Principle 1. Impacting air flows create higher surface pressures.

Principle 2. Diverging air flows create lower surface pressures.

Principle 3. Air flowing from higher to lower pressures at the speed of sound extends lift pressures along streamlines, dissipates lift pressures across streamlines, and interacts with air flow to turn streamlines.

Experimental validation is historically a common validation metric. Types of experimental validations include: wind tunnel studies, studies at steady-state conditions, studies designed to evaluate stability, studies designed to evaluate control surfaces, scaled prototype studies, and studies toward receiving FAA (Federal Aviation Administration) approval. In every phase of experimental validation, there

is either an additional phase of experimental validation or improvement in a prototype that can be performed.

A goal of advanced CFD studies is to proceed directly to scaled prototypes after CFD studies have achieved diminishing returns and optimal designs based on results-driven objectives. Measurement of pressures and velocities at strategic locations on the prototypes would then provide feedback comparison to CFD results.

The Three Principles partially define a new paradigm in vehicle design. A second paradigm of this work is the use of aerodynamic suspension to displace wheeled suspension and its associated rolling/mechanical losses. The generation of "free" aerodynamic lift enables the second paradigm and a key aspect of the work and technology. The claims of 80% reduction in energy consumption are founded in the elimination of substantial rolling losses in combination with further reductions in aerodynamic resistance.

The objective of this work is to convey improved understanding along with digital prototype performances. The goal is rapid progress in transit technology with substantial benefits, including: reduced transit costs, times, carbon emissions, and environmental impacts. The expanded use of electric vehicles is a critical part of realizing the benefits of transit revolution.

The objectives of this study are two-fold: a) use 2D simulations to screen wing section designs for a lifting-body ground-effect vehicle (LB-GEV) design and b) validate and evolve the method to efficiently screen 2D designs toward achieving optimal digital prototype performance. Toward the second objective, the results are presented in the chronological order of investigation in the following sequence:

1) Evaluate a matrix of four airfoil sections at various Source powers, thickness ratios, and ground clearances,

2) Expand studies on a subset of designs to better understand anomalous behavior, and,

3) Evaluate 3D digital prototypes of the two best wing sections at two aspect ratios.

3. Methods

OpenFOAM CFD software was used to simulate digital prototypes from prepared STL files. Methods were matched to maintain fidelity and methods analogous to those within the field [28]-[31]. The turbulence model is k-ω SST. Two-dimensional (2D) simulations were used to identify trends in performance while three-dimensional (3D) simulations were performed on the final prototypes and key designs. Unless otherwise reported, the scale chords of the STLs were 1 m, the fluid was air at 1 atm pressure, and the free stream velocity was 40 m/s. Pressure profiles are symmetrically presented with blue as low pressures, red as high pressures, and passing through green at 0-gauge pressure. Pressure scales are −1000 to 1000 kinematic pressure, m^2/s^2; **Figure 1** uses −800 to 800 for enhanced visualization.

For ground effect simulations, the ground was simulated as a lower boundary condition with a velocity equal to the free stream air. Propulsion sources are modelled as rectangular prisms. Other boundary conditions are modelled as free stream flow at a minimum of 10 chord lengths from the STL.

The Source in a CFD experiment is a selected zone of space where momentum is injected into the flow stream, simulating the increased velocity provided to air traveling through a fan. The source does not model the physical components and direction of airflow through fan blades and housings, which are 3D components, nor the energy inefficiencies of the fan for any related energy analysis related to power requirements for functionality. The source, as much from modelling as from differences between fans and sources, does not inherently provide limitations to the magnitude of injected momentum in comparison to commercially available fans. Therefore, sources with too high a setting are unrealistic, which contributes to factors which exaggerate theoretical performances to 2D simulations.

2D simulations are referred to as being performed on airfoils or wing sections. 3D simulations are referred to as being performed on digital prototypes.

3D digital prototypes have vertical fences which are downward extensions of vertical sides. The heights of digital prototypes are reported based on the horizontal part of the lower surface and do not include ducted fans, fences, or trailing flaps. A trailing section of lower surfaces with increased pitch is considered a flap. In the absence of further clarification, the ratio of fence extension to GEFT height is approximately 0.125 and the ratio of flap extension to GEFT height is approximately 0.1.

OpenFOAM simulation reports lift and drag coefficients based on the same reference value for area which may be different than the scale of anticipated GEFT vehicles. To the first approximation, within 1 - 2 orders of magnitude, the simulation results are independent of scale and are typically performed at 40 m/s with a chord near 1 m in length. Unless otherwise stated, source boxes are 0.02 m tall, 0.002 m deep, and have width equal to the vehicle's width.

OpenFOAM provides values of pressure, velocity vectors, and turbulence at the mesh points of the field. OpenFOAM also reports integrated quantities including lift coefficient, drag coefficients, kinetic turbulence (k), and viscous turbulent energy. OpenFOAM simulation reports lift and drag coefficients based on the same reference value for area, which is set as the planform area.

Figure 1 provides a representative pressure contour which illustrates the formation of a robust pressure along the lower surface to provide lift. The trailing-section upper-surface ducted fan is simulated as a velocity "Source." The formation of the robust lower-surface lift pressure is a result of the manner in which that Source changes the pressure contour over the entire vehicle.

The focus of the CFD simulations is on 2D simulations to evaluate wing section shape, Source power, and thickness ratio (TR). The sequence of analysis includes: a) identifying the Source setting for minimal turbulence, b) comparing thickness ratios at these optimal conditions to identify an optimal thickness ratio, and c)

performing 3D digital prototype experiments to determine how 2D simulations correlate with digital prototype performances.

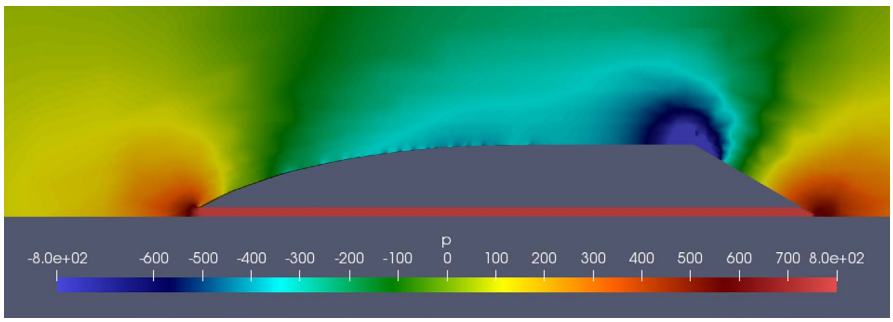

Figure 1. Illustration of pressure contour, m^2/s^2, of GEFT with robust pressure in lower cavity.

Figure 2 identifies the wing sections evaluated in this paper. A research emphasis to identify a minimum in the volumetric averages of kinematic turbulence (k) as a basis for identifying optimal configurations and operating conditions. Source setting (m^4/s^2) is an operational parameter. The value of the Source setting is less important than the optimal conditions, such as L/D efficiency, at the optimal Source setting.

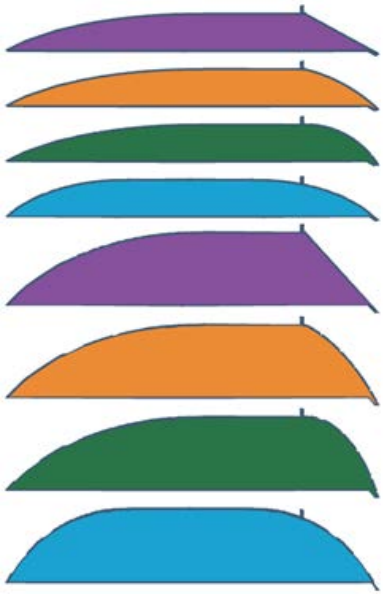

Figure 2. STL wing section models at 0.1 (top) and 0.2 (bottom) thickness ratios (TR) used for simulation from top to bottom: a) flat taper, b) low (convex) camber taper, c) high camber taper, and d) long camber taper. Graphs are color-coded to match the wing sections and Sources (e.g., ducted fans) in rectangular configuration on the upper surfaces at the onset of the trailing tapers.

4. Results

Data from an initial screening matrix of 2D simulations was processed to identify

the values of Source power for minimums in kinematic turbulence (k), graphed in Figure 3. Except for the long camber taper wing section, the minimum in k was achieved at Source powers between 10 and 50. Turbulence initially decreases with increasing Source powers due to mitigating boundary layer separation (BLS) at the onset of the trailing taper. The 0.1 TR long camber taper wing section did not exhibit BLS.

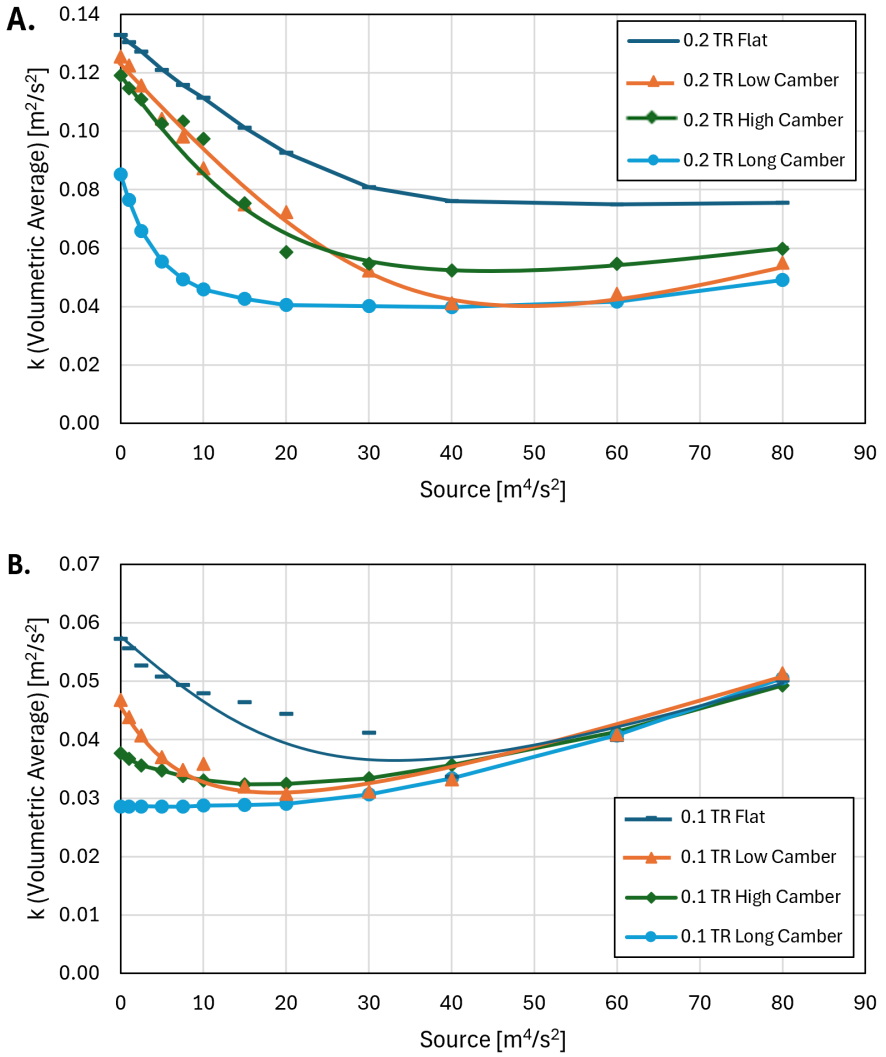

Figure 3. Volumetric average kinetic turbulence (k) as a function of source setting for 0.2 (A) and 0.1 (B) Thickness Ratio airfoils. All data are at 40 m/s for the air.

The optimization path associated with minimums in k preferred performance at a Source setting corresponding to 80% of the decrease in k ("80% k," the difference taken between the initial, 0 Source, value and minima in k). The value at 80% decrease in k magnitude provided more consistent source and L/D identification than at the minimum in k since k often has a broad flat minimum with regards to Source—80% k is referred to as the "optimal value" primarily as a convenience in discussion rather than the rigorous accuracy of such characterization. Due to the

flat minima in kinematic turbulence with respect to source, 80% k is a more consistent value to obtain for comparison. Figure 4 compares the 80% k values divided by TR as a function of TR.

Each data point of Figure 4 is based on about a dozen 2D simulations at different Source settings to identify the "optimal" performance for each wing section. The optimal source settings for each wing section are the conditions of interest for comparison.

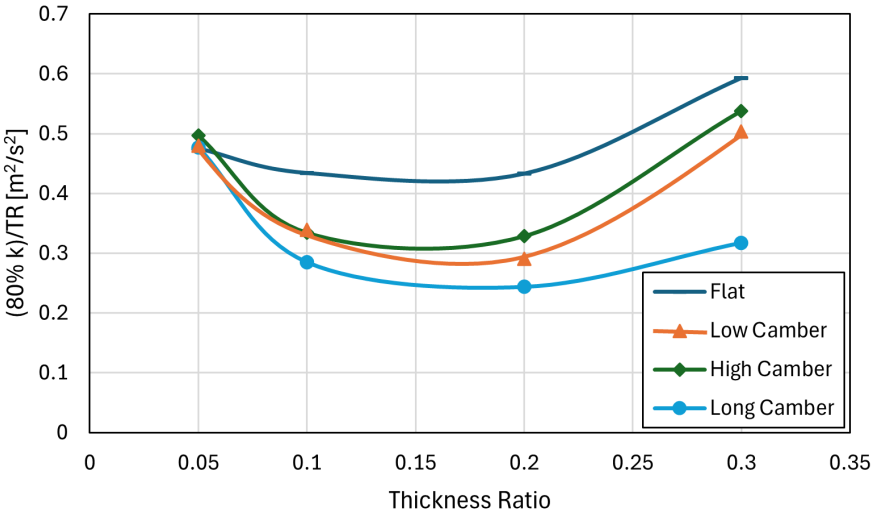

Figure 4. Volumetric average kinetic turbulence (k) divided by Thickness Ratio (TR) as a function of Thickness ratio (TR) for each airfoil. The airfoils are compared at the condition determined as 80% of the value of k from the difference between the kinetic turbulence without an active source and the minimum of kinetic turbulence.

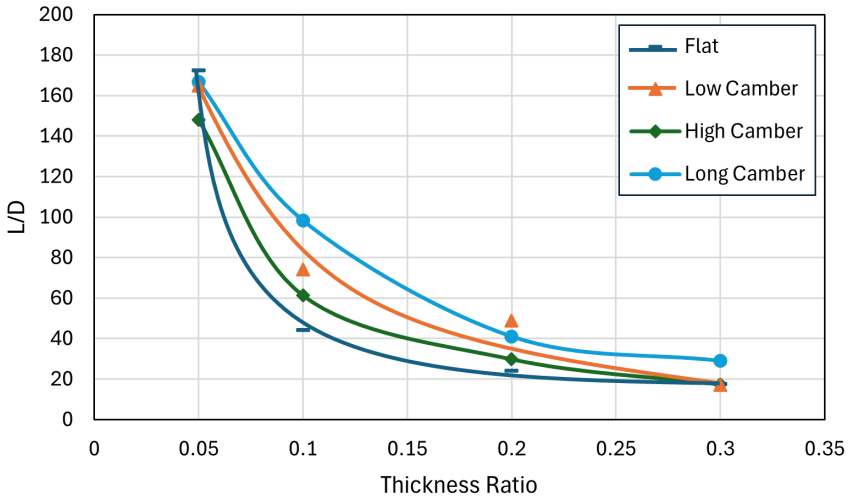

Figure 5. Lift to drag ratio (L/D) as a function of Thickness ratio for each airfoil. The airfoils are compared at the condition determined as 80% of the value of k from the difference between the kinetic turbulence without and active source and the minimum of kinetic turbulence.

The performance curves of Figure 4 nicely distinguish the better-performing

wing sections. The L/D efficiencies corresponding to Figure 4 conditions are provided by Figure 5. The trend of increasing L/D with decreasing TR has limited practical value in the limit of low TR and maximum L/D. Low cabin heights of thin lifting bodies have limited practicality for passengers and freight.

Dividing 80% k values by TR converts the overall turbulence to turbulence per wing section, corresponding to turbulence per volume in 3D. 80% k/TR is a volume-specific value with optimal volume-specific values between TR of 0.1 and 0.2.

The L/D values show consistency in trends. L/D decreases with increasing TR and consistently maintains values above 20 up to 0.2 TR. The Source powers corresponding to Figure 4 conditions are summarized by Figure 6.

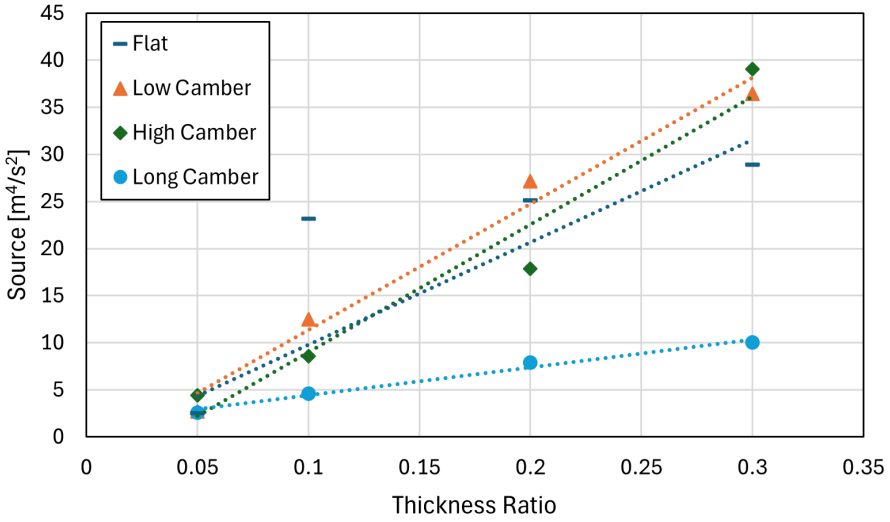

Figure 6. Source settings versus TR. Each data point is at its respective optimal Source setting based on six to twelve wing section simulations for 80% k.

4.1. Additional Studies

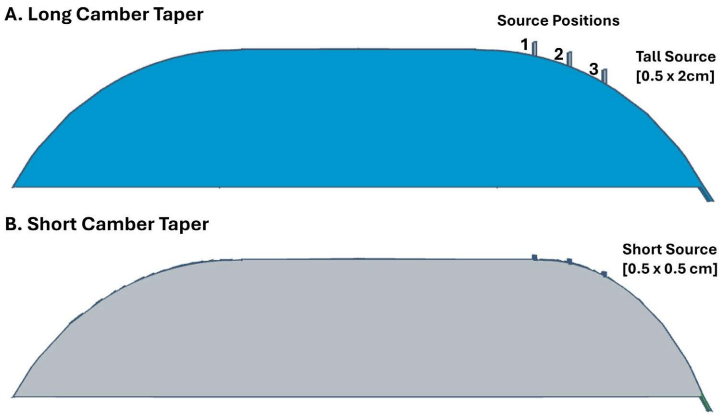

Figure 7. Schematic of 0.2 TR airfoils designed to analyze the impact of source size and location: the Long Camber taper, (A) is the same as the 4th design in other experiments; B is a modification for a Short Camber taper. There are 3 locations for each source at approximately c = 0.75 (1), c = 0.8 (2), and c = 0.85 (3). The Sources are 0.5cm wide and either 0.5 cm high (short) or 2 cm high (tall). Previous figures use tall sources in position 2.

Earlier studies on GEFT identified the optimal Source location at the onset of the taper [32]. The results of this study provide more nuance for this, with the best performance associated with the Source located slightly beyond the taper's onset. Variation in both the location and the height of the source may have some potential. Additional 2D studies designed to investigate this anomalous behavior were performed on the Source variations summarized by **Figure 7**. **Figure 8** summarizes the results of these additional 2D studies.

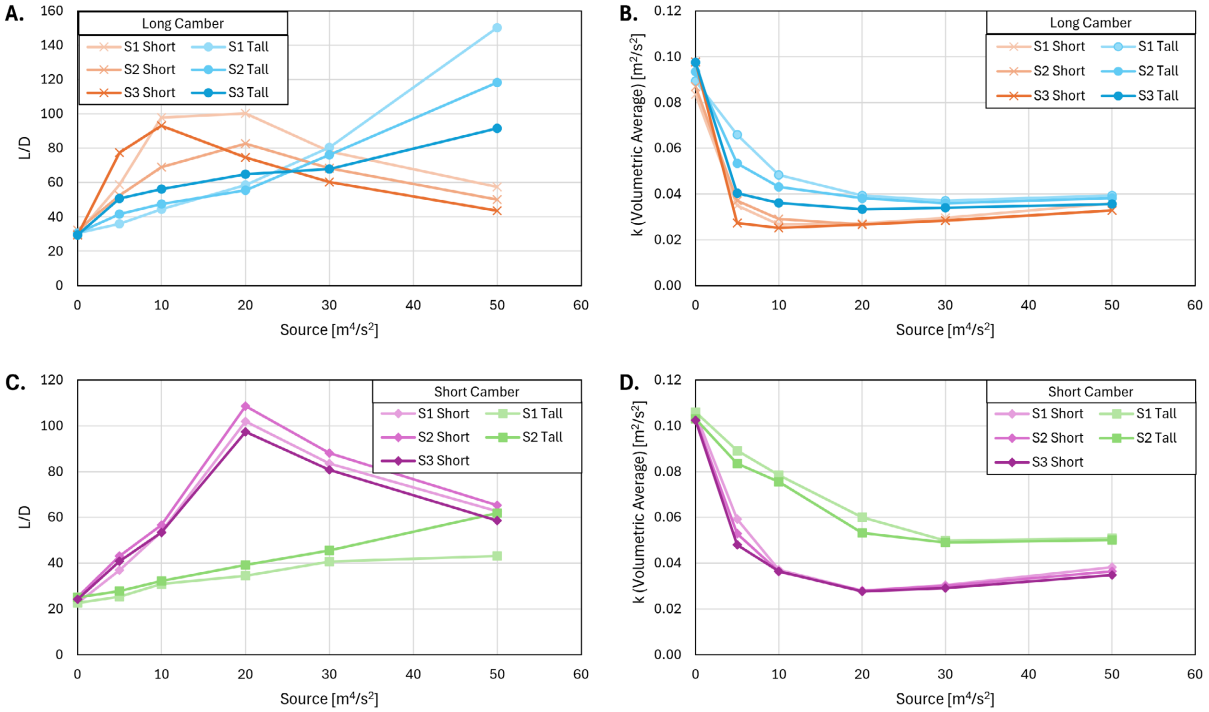

Figure 8. Results for the different positions and sizes of sources on the airfoils of **Figure 7**. L/D is on the left and the volumetric average of k is on the right. The Long Camber Taper is graphed on A and B. The Short Camber Taper is graphed on C and D. Short sources (0.5H) are warm colors (orange and purple); Tall source (2H) are cool colors (blue and green). The different positions are shaded from lighter (1) to dark (3).

A summary of the additional findings of **Figure 8** variations in Source height and locations are:

1) The shorter (lower height) Source consistently produces lower turbulence and higher L/D.

2) The minimum in turbulence, as associated with optimal performance, occurs at lower Source settings for the shorter Source with diminished performance (*i.e.*, lower L/D and higher turbulence) after the minimum in turbulence.

3) An explanation for diminishing performance after a minimum in turbulence for the shorter Source is that the higher velocities of discharge diverge from the taper and create lower pressures.

4) The longer camber taper decreases turbulence and increases L/D versus the shorter taper and is the primary reason the long camber wing section of **Figure 2** exhibits superior performance.

5) As the Source power increases, improved performance was realized by placing the Source higher up on the trailing taper; this is due to lower lift-induced drag at the Source intake.

6) The long camber taper better utilizes the inherent ability of the air flow to follow curvature without supplement from a Source; this is why a longer camber along the chord with a slight taper performs better than shorter alternatives. It is likely that a modest step-change increase in pitch between the Source intake and discharge has an optimal performance, but this highlights the optimization needed between shorter tapers and lower pitch tapers.

7) The sudden change in pitch on the shorter camber is likely associated with low L/D performance (and higher turbulence) resulting from not overcoming boundary layer separation until higher pressures are generated over the trailing taper leading to an artificial increase in L/D exceeding 100.

8) As the Source power increases, k tends to converge on the same line; this is likely due to jetwash-dominated turbulence. Increased L/D in this range is due to induced thrust on the vehicle surface at the expense of momentum-based thrust from the Source, which is not a practical option for operation.

9) The taller sources have better performance at low locations on the taper due to reduced intake choking along the initial slope of the taper.

Lower turbulence with longer taper distances was an anticipated trend, but an optimal chord length is a balance of higher efficiency versus a greater fraction of the wing section at the maximum thickness/height. A recurring observation in GEFT optimization is that higher, longer cabin volumes decrease higher L/D efficiency.

Table 1 summarizes the key performance parameters for the 2D studies identified as optimal Source settings. The lift coefficients are consistently between 1.37 and 2.0 at the optimal setting. The higher L/D are a result of decreasing pressure drag.

Table 1. 2D of ideal interpolated 80% k values (graphed data, Figures 4-6).

Taper	Thickness Ratio	Source (m^4/s^2)	L/D	Cl	Cd	K (m^2/s^2) (Volumetric Average)
Flat Taper	0.05	2.5	172.6	1.92	0.0111	0.024
Flat Taper	0.1	23.2	44.3	1.37	0.0310	0.044
Flat Taper	0.2	25.1	24.2	1.66	0.0687	0.093
Flat Taper	0.3	28.9	17.8	1.81	0.1015	0.209
Low Camber	0.05	2.7	164.9	1.92	0.0117	0.024
Low Camber	0.1	12.5	74.2	1.58	0.0213	0.036
Low Camber	0.2	27.2	48.9	1.77	0.0362	0.072
Low Camber	0.3	36.5	17.0	1.81	0.1062	0.180
High Camber	0.05	4.4	147.9	1.93	0.0131	0.025
High Camber	0.1	8.6	61.3	1.49	0.0243	0.034

Continued

High Camber	0.2	17.9	29.8	1.68	0.0564	0.075
High Camber	0.3	39.0	17.4	1.81	0.1043	0.183
Long camber	0.05	2.6	166.7	1.90	0.0114	0.024
Long camber	0.1	4.6	98.4	1.54	0.0156	0.029
Long camber	0.2	7.9	41.1	1.78	0.0433	0.049
Long camber	0.3	10.0	29.1	2.01	0.0690	0.095

4.2. 3D Studies

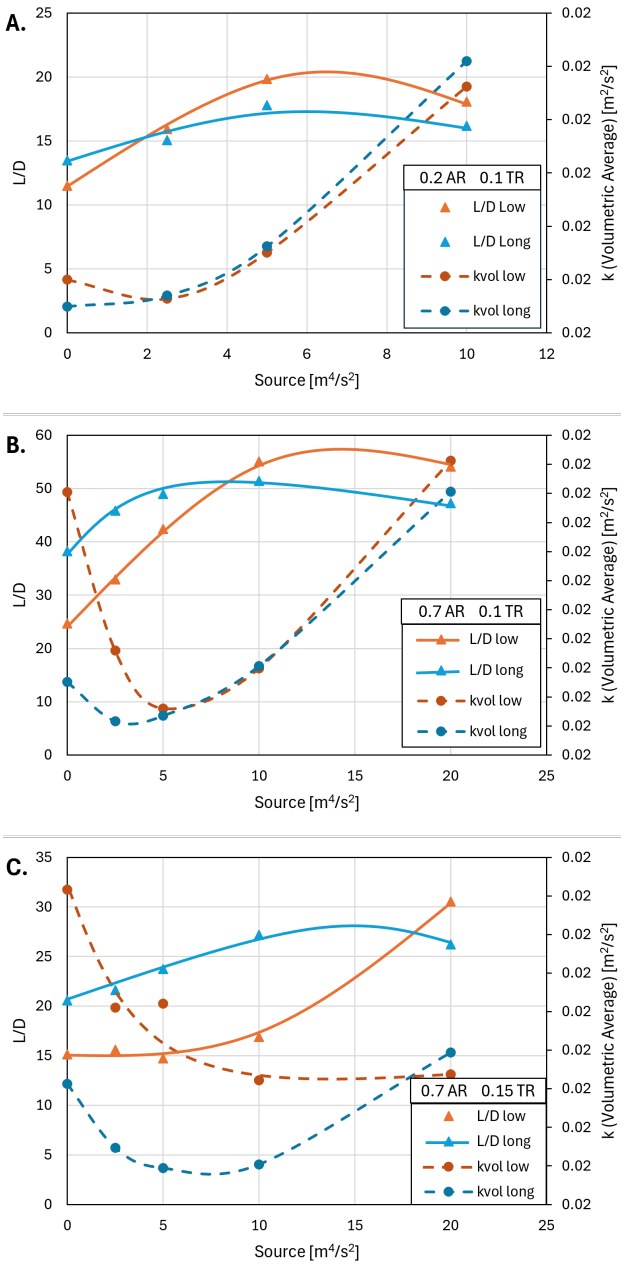

Figure 9. 3D performance: a) 0.2 AR, 0.1 TR; b) 0.7 AR 0.1 TR; and c) 0.7 AR 0.15 TR. Results include data for both low and long camber taper digital prototypes.

The wing sections studied identified the long camber and low camber designs of Figure 2 as optimal for further studies in 3D. The low camber design provided a local optimum between the flat and high camber tapers, maintaining the larger cabin. The long camber represents a surface ideal with less boundary layer separation. The following are the additional parameters for 3D studies:

1) Fences are at a constant ground clearance ratio of 0.02 (*i.e.*, clearance 2% of the wing section thickness), a cavity height of 12.5% of the wing section thickness, and a flap set to span 80% of the cavity height (10% of the wing section thickness) as a continuation of the slope of the trailing taper.

2) Thickness ratios (TR) at 0.1, 0.15, and 0.2.

3) Aspect ratios (AR) of 0.2 and 0.7.

The 3D studies are summarized by Figure 9. The expectation of the long camber wing section to have higher L/D than the low camber is supported by the 0.7 AR results, but the 0.2 AR results for the two wing sections are similar both in L/D and turbulence with the maximum L/D near 20.

The pressure contours of Figures 10-11, as well as the summary of C_l in Table 2, provide the insight that at AR = 0.2 the higher pressures in the lower cavity are not fully developed.

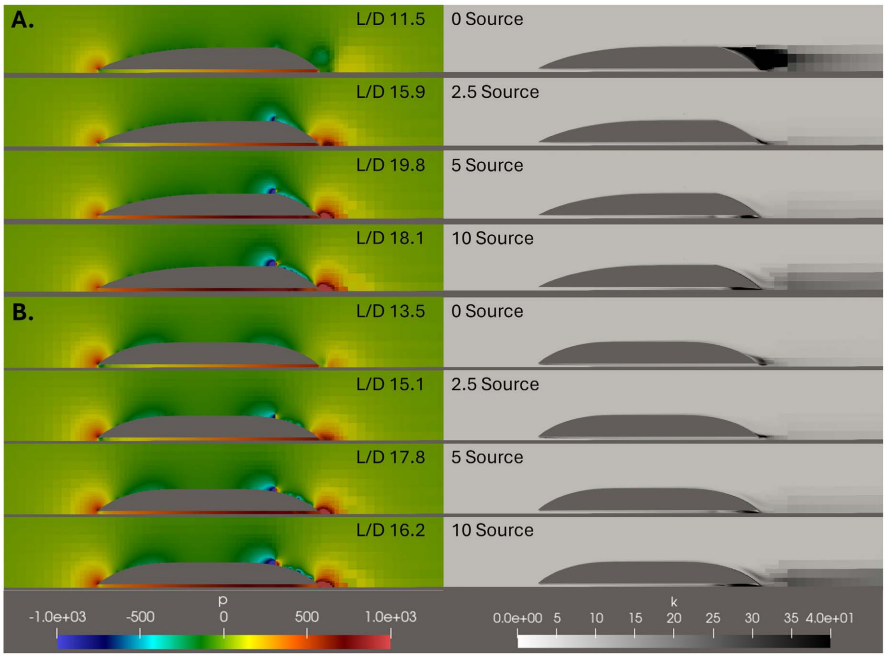

Figure 10. 3D digital prototype midline pressure (left) and turbulence (right) contours for: A) low camber 0.2 AR, 0.02 GR, 1.25x Fence, 0.1 TR; and B) long camber at .02 GR, 1.25x Fence, 0.1 TR.

Figure 10 identifies that in 3D, the pressure expands from the back forward through the development of the pressure contours within the cavity. C_l less than approximately 1.1 (see Table 3) identify that the lower cavity pressure contour is not fully developed. The primary cause for the lack of development is the lateral

losses of pressure under the fences.

The likely cause for similar performances between the two wing section designs at the 0.2 aspect ratio is that performance is dominated by the lateral losses of the higher pressures in the lower cavity. As the aspect ratio increases, the performances are impacted more by the features of the airfoil shape, as identified in the 2D studies.

For both models, as the Source setting increases turbulence matures from boundary layer separation above the trailing taper, to a minimum in observed turbulence, and finally to the development of jet wash turbulence behind the taper. The jet wash turbulence is typically next to the ground at a height of about half the vehicle height.

The lower curvature and taper pitch of the long camber model leads to less boundary layer separation with correspondingly higher L/D efficiency and lower Source settings at optimal conditions. At the highest Source settings, the higher pitch at the Source intake leads to lift-induced drag and slight decreases in L/D efficiency.

Figure 11. 3D digital prototype midlines for 0.7 AR data. A: Low camber 0.02 GR, 1.25x Fence, 0.1 TR; B: Low camber 0.02 GR, 1.25x Fence, 0.15 TR; C: Long camber 0.02 GR, 1.25x Fence, 0.1 TR; D: Long camber 0.02 GR, 1.25x Fence, 0.15 TR.

The turbulence patterns of the AR = 0.7, TR = 0.1 wing section of **Figure 11** qualitatively follow the same trends as **Figure 10** wing section at AR = 0.2. However, at the higher AR of 0.7, higher pressures develop in the lower cavity with correspondingly higher L/D efficiencies.

Differences between the low camber and the long camber models begin to emerge as the thickness ratio increases from 0.1 to 0.15 as seen in the right portion of **Figure 11**. The long camber model maintains reasonable L/D at the greater thicknesses, however, trailing turbulence becomes significantly more noticeable. The low camber model has worse L/D than the long camber model to the extent that it exhibits an atypical, relatively constant L/D at Source settings from 0 to 10. However, higher Source settings eventually overcoming the boundary layer

separation, but the L/D efficiency is less than anticipated relative to the long camber wing section, though it still exceeds the long camber model's L/D at high sources.

Table 2. Summary of performance parameters for the 3D CFD simulations.

Taper	Source (m^4/s^2)	L/D	Cl	Cd, Viscous	Cd, Pressure	K (m^2/s^2) (Volumetric Average)
			TR = 0.1, AR = 0.2			
Low Camber	0	11.5	0.42	0.0084	0.0282	0.0208
Low Camber	2.5	15.9	0.59	0.0096	0.0275	0.0208
Low Camber	5	19.8	0.92	0.0100	0.0365	0.0209
Low Camber	10	18.1	0.99	0.0117	0.0429	0.0212
Long camber	0	13.5	0.47	0.0088	0.0262	0.0207
Long camber	2.5	15.1	0.57	0.0099	0.0282	0.0208
Long camber	5	17.8	0.85	0.0106	0.0372	0.0209
Long camber	10	16.2	0.91	0.0126	0.0437	0.0212
			TR = 0.2, AR = 0.2			
Low Camber	0	3.6	0.47	0.0120	0.1183	0.0214
Low Camber	5	5.2	0.86	0.0135	0.1536	0.0215
Low Camber	10	4.9	0.95	0.0150	0.1765	0.0216
Low Camber	20	4.5	1.05	0.0172	0.2174	0.0221
Long camber	0	3.6	0.41	0.0122	0.0996	0.0214
Long camber	5	4.6	0.76	0.0139	0.1526	0.0216
			TR = 0.1, AR = 0.7			
Low Camber	0	24.7	0.87	0.0053	0.0301	0.0217
Low Camber	2.5	33.0	0.94	0.0057	0.0227	0.0212
Low Camber	5	42.4	1.00	0.0060	0.0175	0.0210
Low Camber	10	55.1	1.08	0.0064	0.0133	0.0211
Low Camber	20	54.1	1.45	0.0064	0.0205	0.0218
Long camber	0	38.2	0.97	0.0055	0.0199	0.0211
Long camber	2.5	45.8	1.03	0.0058	0.0167	0.0209
Long camber	5	49.0	1.07	0.0061	0.0156	0.0209
Long camber	10	51.4	1.15	0.0067	0.0157	0.0211
Long camber	20	47.3	1.42	0.0072	0.0229	0.0217
			TR = 0.15, AR = 0.7			
Low Camber	0	15.1	0.91	0.0056	0.0549	0.0230
Low Camber	2.5	15.6	0.94	0.0057	0.0543	0.0224
Low Camber	5	14.7	1.00	0.0058	0.0622	0.0224
Low Camber	10	16.9	1.00	0.0063	0.0529	0.0220

Continued

Low Camber	20	30.6	1.55	0.0067	0.0439	0.0221
Long camber	0	20.6	1.02	0.0054	0.0441	0.0220
Long camber	2.5	21.6	1.07	0.0056	0.0441	0.0217
Long camber	5	23.7	1.12	0.0058	0.0413	0.0216
Long camber	10	27.2	1.22	0.0063	0.0387	0.0216
Long camber	20	26.2	1.53	0.0069	0.0513	0.0222
			1˚ pitch, TR = 0.1, AR = 0.2			
Low Camber	0	18.4	0.83	0.0081	0.0374	0.0208
Low Camber	2.5	20.3	0.95	0.0092	0.0376	0.0208
Low Camber	5	20.4	1.03	0.0097	0.0410	0.0209
Low Camber	10	17.7	1.16	0.0108	0.0545	0.0212
Long camber	0	19.6	0.88	0.0084	0.0364	0.0208
Long camber	2.5	19.4	0.96	0.0097	0.0396	0.0208
Long camber	5	18.8	1.12	0.0104	0.0491	0.0209
Long camber	10	16.8	1.15	0.0125	0.0557	0.0212

Table 2 parameters identify the low camber digital prototype has similar viscous drag coefficients as the long camber airfoil at TR = 0.15, but higher pressure drag at the lower sources. The cause of the lower L/D is primarily due to lower lift coefficients. Further studies to better isolate the slightly diminished performance are outside the scope of present studies.

4.3. Additional 3D Studies

The good performance of GEFT consists primarily of two simultaneous developments in the pressure and turbulence contours around the wing section:

1) Firstly, the Source pushes more air above the taper resulting in mitigation of the boundary layer separation, reducing pressure drag.

2) Secondly, the formation of the trailing-region stagnation region leads to higher pressures expanding into and forward through the lower cavity—increasing C_l to values between 1.1 and 1.4.

The 0.2 AR wing sections of Table 2 failed to achieve $C_l > 1.0$ due to the lateral loss of lift pressures between the fences and the ground. Additional simulations were performed at a 1˚pitch on the lower cavity with the fences maintaining a constant ground clearance. Figure 12 provides pressure contours for 3D digital prototypes at 1˚pitch.

The addition of a 1˚pitch to the lower surface, at a constant fence clearance, provides consistently robust higher pressures in the lower cavity. The beneficial impact was greater at zero Source setting where L/D increased from 11.5 and 13.5 to 18.4 and 19.6 respectively for the Low Camber and Long camber designs.

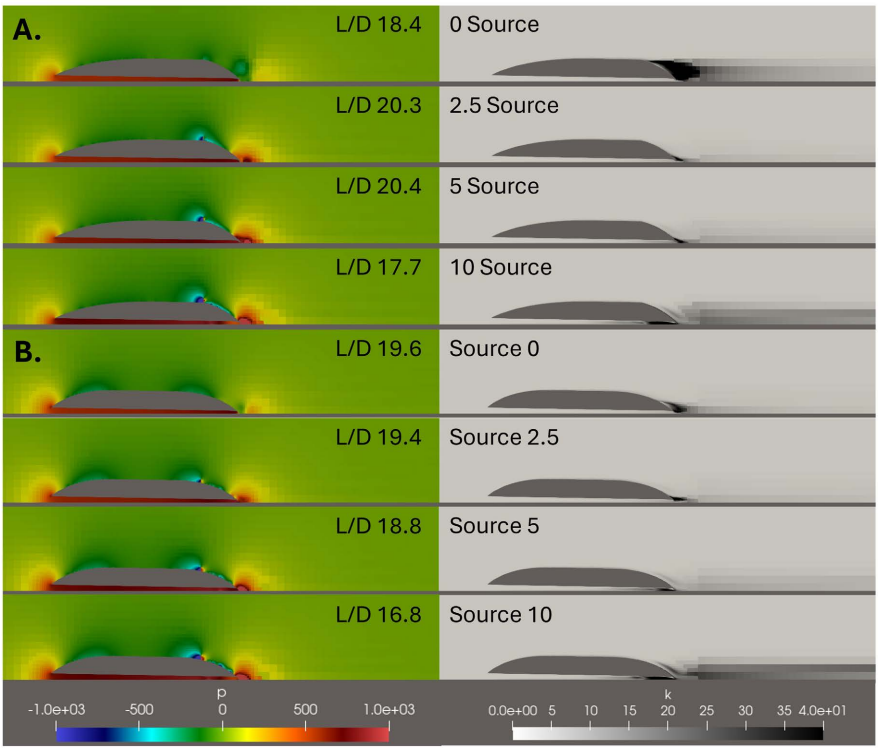

Figure 12. 3D digital prototype midline pressure (left) and turbulence (right) contours for: A) TOP low camber 0.2 AR, 0.02 GR, 1.25x Fence, 0.1 TR at 1˚pitch; and B) long camber of .02 GR, 1.25x Fence, 0.1 TR at 1˚pitch.

4.4. Lower Velocity Studies

Additional simulations were performed at 20 and 30 m/s to verify that performance patterns at 40 m/s were also present for typical cruising velocities of highways. Figure 13 provides pressure profiles and Figure 14 illustrates the minimum in k as Source power increases. The minimum in k is verification that the Source settings and GEFT designs follow similar trends at the lower velocities as the 40 m/s data of this paper.

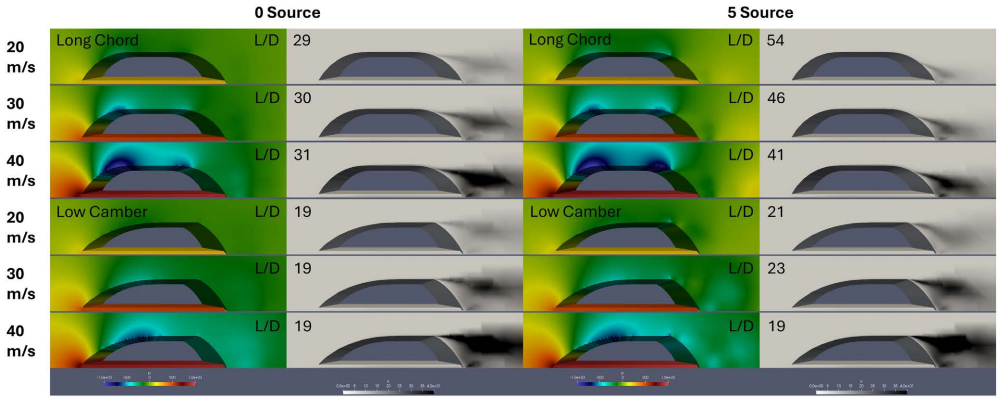

Figure 13. Pressure contours for 0.2 Thickness Ratio airfoil simulations at 20 and 30 m/s. Sources: left 0 m^4/s^2, right 5 m^4/s^2. The upper half is the long camber GEFT design while the lower half is the low camber GEFT design.

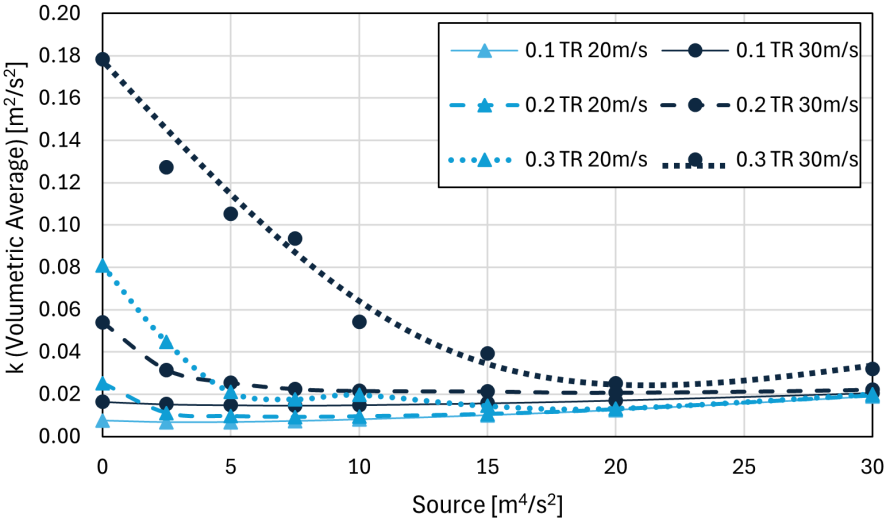

Figure 14. Graphical illustration of minimum in k as Source power increases. Data provided for the long camber and low camber GEFT airfoil designs for 20 and 30 m/s at 0.1, 0.2, and 0.3 TR.

The development and expression of turbulence remains the same at the lower velocities. Two differences appear within the dynamics of lift generation, turbulence development, and boundary layer separation mitigation. The lower velocity has less dynamic pressure, therefore producing less total lift when converted into static pressure within the cavity. Conversely, the lower Reynold's numbers of the 20 and 30 m/s velocities produce less turbulence [33]-[38]. Therefore, lower source settings are able to overcome and mitigate the boundary layer separation that develops, leading to better efficiency from the upper-surface trailing propulsor.

5. Discussion

5.1. Identifying Optimal Performance

The strategic location of propulsion at upper-surface trailing-section locations in GEFT configurations provides unique and valuable performance aerodynamics. The addition of thrust to the propulsor-wing section configuration reduces lost work. In optimal designs, initial power to the propulsors both provides thrust and reduces turbulence, as can be measured by the CFD turbulence parameter k. Continued increases in propulsor power ultimately lead to more propulsion energy manifesting as jet wash rather than favorable changes in pressure on the vehicle surface. Initially, the jet wash may be seen in the form of higher-flow laminar streamlines with the peak velocities approximately 10% of the vehicle's height above the ground. This laminar flow is lost work which can be better detected through k measurements as it transforms into turbulent flow over time.

Volume-specific k for the entire mesh consistently yields a minimum in k as power increases to GEFT's upper-surface trailing-section propulsor in 2D simulations. This behavior leads to the following computational sequence to compare

vehicle wing section shapes and thickness ratios to identify optimal shapes and thickness:

Step 1. Simulate 2D wings section aerodynamics while recording data on k versus Source power.

Step 2. Identify the minimum k as a function of Source power (e.g., Figure 9) alongside collection of k, L/D, TR, and additional data for Step 3 at a specified value of k (*i.e.* 80% k).

Step 3. Compare the performances of different wing section shapes using k/TR as the y-axis metric and TR as the independent variable (e.g., Figure 4).

The wing section exhibiting the minimum of k/TR metric is a preliminary estimate for the wing section with the best performance balanced with TR functionality.

Key aspects of the analysis include:

1) To divide k by TR to get vehicle volume-specific performance to avoid skewing optimal L/D efficiency to the lowest thickness ratio which is too thin to be of practical value for most payloads.

2) The most energy efficient designs have performance curves exhibiting lower k/TR.

Three of the four wing sections of Figure 2 have trailing tapers starting at 0.8 chord lengths from the leading edge of the vehicle. The fourth wing section, the long camber taper, has a trailing taper starting at about 0.7 chord lengths from the leading edge of the vehicle.

The best performers of the initial experimental matrix (Figure 4) had low convex-upward cambers. The wing section with the taper starting at the more-forward position of 0.7 chords has the lowest overall turbulence with the unexpected result that this performance was achieved with a source at the 0.8 chord position. Further studies were performed to confirm the validity and identify a basis for better performance with a Source located partially down the trailing taper. However, optimal Source location is a function of Source setting with higher Source locations generally corresponding better performance.

The local L/D efficiency at the vehicle's surface immediately forward the intake is 57˚/α˚. Therefore, in theory if the target L/D efficiency is > 22, the intake surface immediately before the intake should have a pitch of less than 2.5˚ so as not to lead to an adverse contribution to overall L/D efficiency.

Additional studies located the source extending further vertically from the upper surface at 0.7, 0.75, and 0.8 chord lengths. Performance was similar for all these source positions at lower source powers, indicating the reason for improved performance was the lower average pitch of the trailing taper. The use of a lower average pitch taper has advantages for reduced lost work. Disadvantages of a higher-pitch camber include reduced cabin length of maximum height, and, potentially, a less-robust trailing edge stagnation region.

A broadly applicable conclusion from these studies is that a low camber (around 4%) on the trailing taper surface leads to improved performance. A low camber

on the trailing taper reduced the propensity for boundary layer separation, which can improve efficiency and reduce reliance on Source power to overcome the boundary layer separation.

5.2. Visual Verification

The reliability of determining operating and comparison conditions for GEFT based on patterns in k development as source increases is dependent upon registering both: a) turbulence from boundary layer separation around the airfoil and b) turbulence from jetwash behind the taper. Figure 15 provides pressure contours and k contours for airfoils at different source powers to provide visual confirmation that k registers both forms of lost work. At low source values, large quantities of turbulence may be seen, which tapers off as the optimal identified source is approached. After increases in source power beyond optimal conditions, the jetwash development becomes visible in the far field as the initially laminar streamlines begin to mix with the surrounding air to produce turbulence, confirming that k identifies jetwash as lost energy as well as the boundary layer separation with large Eddy turbulence. Jetwash development can be observed in the plots of volumetric averages of k as the positive slope which appears after the minimum in k.

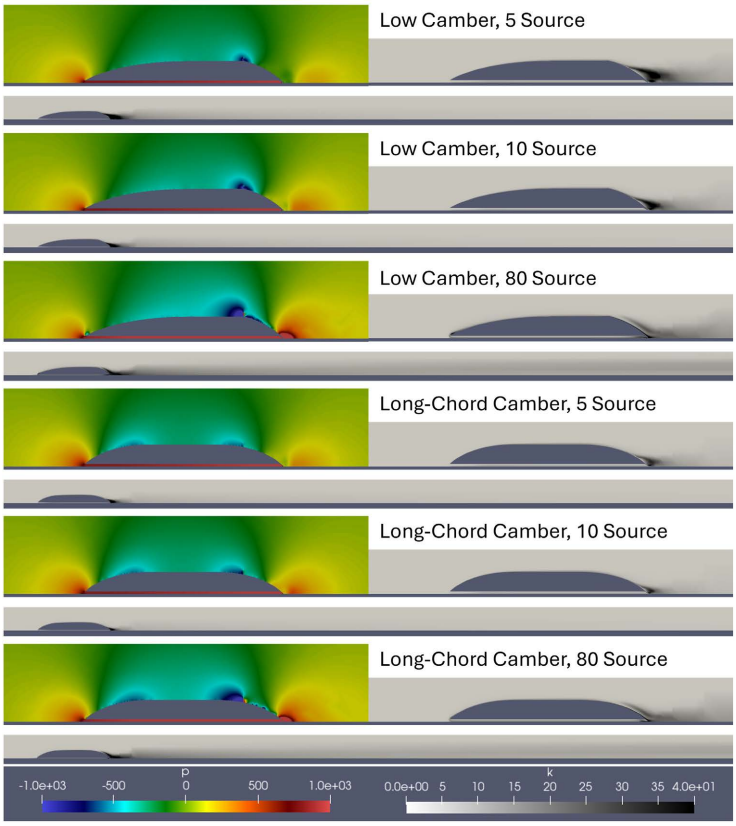

Figure 15. Visual verification of boundary layer separation and jetwash. For both the Low Camber and Long Camber airfoils, pressure contours and k contours are provided around the airfoil as well as an extended k profile to express boundary layer separation. The Extended profiles have a scale of 0 - 20 for k.

While k is able to indicate the presence of jetwash in the simulation, the jetwash's dependence on mixing with lower velocity air to express as turbulence indicates that k is less sensitive to jetwash than other sources of turbulence. Therefore, because jetwash has a lesser impact on the total value of k, it is reasonable to provide the assumption that the ideal operating and comparison condition is at source powers less than the reported minimum of k. The earlier analysis of this paper uses the value of "k 80%" between the initial value (No active source) and the minimum for comparison for this reason.

5.3. Computational Times

The benefits of computational analysis lie in the ability to perform experiments and test variations in designs without the significant cost and effort of modifying physical prototypes. Computational experiments therefore become a balance between complexity and computational power/time. A primary method to maintain validity without excessive computational needs is to have increased mesh nodes at locations close to locations of high fluxes and variations. In particular, there is increased mesh density near the airfoil and walls with a uniform less dense grid farther away. This provides local and global refinement as two separate variables. We can determine both effective local and global refinements to maintain reasonable validity while minimizing computational cost. For example, while maintaining the same overall refinement adjacent to the airfoil, providing similar results for the experiment, reducing the overall mesh grid density can decrease computation time by nearly 90% as seen by Table 3. Figure 16 shows examples of meshes with the same absolute local refinement around the airfoil, but different global mesh densities; these conditions are 250 x-Direction with 5 additional refinement, 500 x-Direction with 4 additional refinement, and 1000 x-Direction with 3 additional refinement. The computational costs can be directly associated with time. There are two notable stages to computational cost for these experiments: development of the background mesh based on an STL with a specific ground ratio and the run time for reaching steady state for the experimental flow.

Table 3. Mesh and Run times for different refinement conditions.

Mesh Refinement		Additional Refinement	Meshing Time (min)	Average Run Time (min)
x-Direction	y-direction			
250	125	3	Fail	Fail
250	125	4	Fail	Fail
250	125	5	1	4
500	250	3	Fail	Fail
500	250	4	1	18
500	250	5	3	20
1000	500	3	7	93
1000	500	4	5	70
1000	500	5	8	71

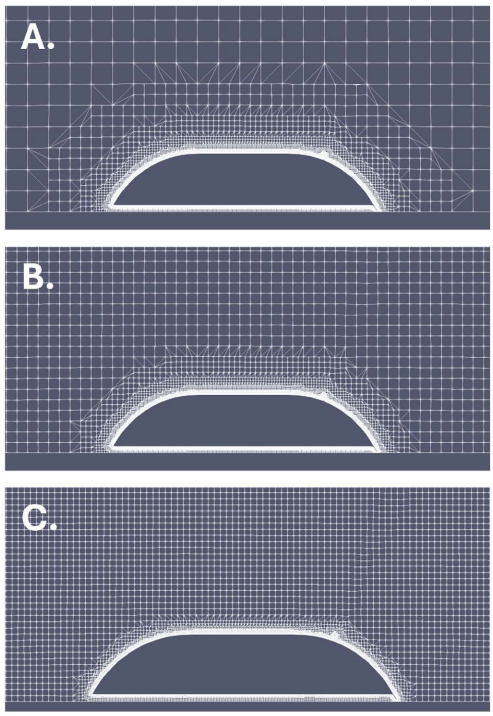

Figure 16. Wing section meshes at different global densities and the same local refinement. A: 250 by 125 global mesh grid with an additional 5 levels of refinement, B: 500 by 250 global mesh grid with an additional 4 levels of refinement, and C: 1000 by 500 global mesh grid with an additional 3 levels of refinement. All meshes have 5 layers of additional boundary layer around the airfoil itself.

The data in this experiment was collected at conditions that had less than 5% deviation from significantly higher mesh conditions when compared at selected reference positions. The method by which values are calculated for field averages within experiments is important and can be affected by the meshing parameters. Particularly for the calculation of kinetic turbulence energy (k), OpenFOAM has functions to calculate the values through either a volumetric average value or the field average value. The volumetric average normalizes the field values of k by the volume of the cells by their respective nodes, which prevents deviations based on differences in the balance between airfoil local mesh refinements and the global mesh as highlighted in Figure 10. However, the field value average of k does not normalize by the volume and therefore is strongly influenced by the balance between global mesh density and localized refinement, providing greater weighting to the field area directly around and in the proximity of the airfoil as seen in Figure 11. For multiple factors, volumetric averages of k are preferred. Volumetric average provides an absolute value independent of these chosen experimental refinements and it is more susceptible to picking up non-reversible lost work, such as jet streams, which appear further out within the field.

5.4. Repeatability versus Accuracy

The results of this paper are based on a volumetrically averaged kinematic turbu-

lence calculation. Figure 17 illustrates the volume average values which can be compared to the field average values of Figure 18. An important difference between the two approaches is that the Source value at the minimum turbulence varies with refinement conditions, ultimately reaching values well beyond 20. The volume average k is more consistent with the turbulence contours, has consistency for identifying the same values at different mesh resolutions with respect to source power, and a more notable minimum.

The volume average turbulence at the minimum value and at 80% k, both have merit based on repeatability. Merit based on absolute accuracy for highest efficiency is a more elusive objective; however, the results of this paper identify that the selected path of consistence has sufficient accuracy so as to be a good starting point for final optimization based on other algorithms, providing an acceptable balance between turbulence and jet wash lost energy.

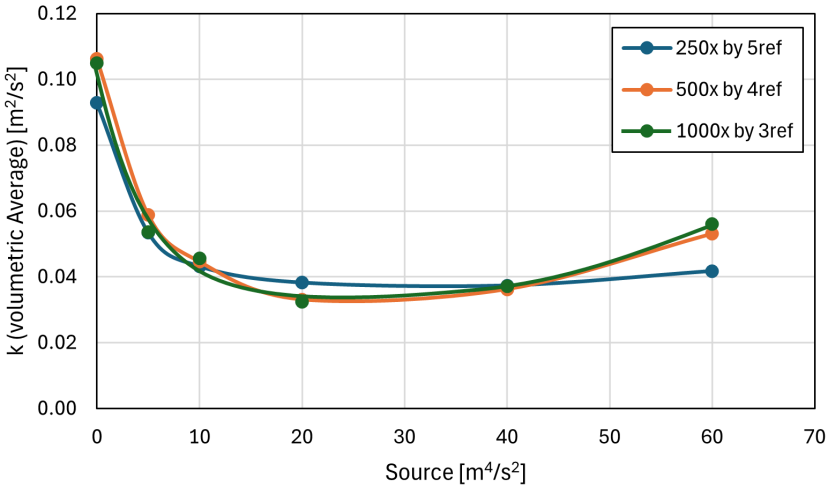

Figure 17. The Volumetric Average of k as a function of source for a long camber taper 0.2 Thickness Ratio airfoil with the same localized refinement, but different global mesh sizes.

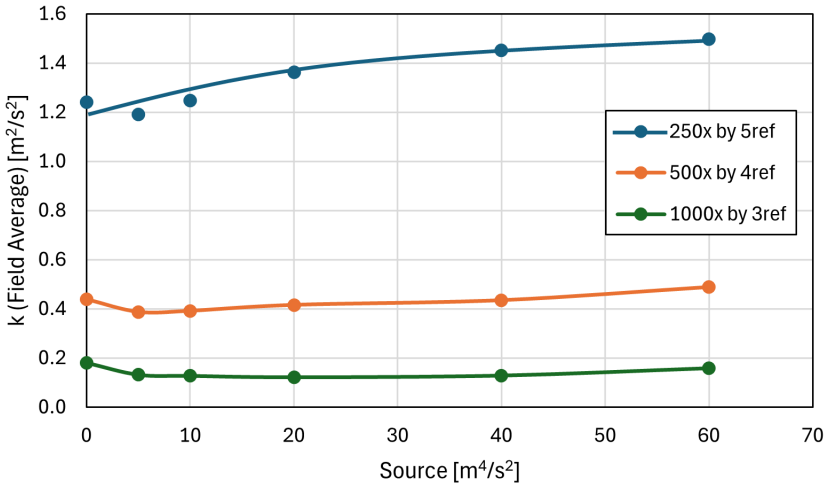

Figure 18. The Field Average of k as a function of source for a long camber taper 0.2 Thickness Ratio airfoil with the same localized refinement, but different global mesh sizes.

Table 4. Simulation times for 3D simulations.

Aspect Ratio	Thickness Ratio	Average mesh time (min)	average run time (min)
0.2	0.1	52	499
0.2	0.2	51	542
0.7	0.1	60	551
0.7	0.15	63	623

Table 4 provides the meshing times and average run times for the different digital prototypes examined. Depending on the chosen condition, the wing sections are 80-99% faster than the digital prototype experiments. Therefore, the choice of a lower refinement, but still reasonably accurate wing section model may provide a wide range of analysis for the identification of ideal digital prototypes to investigate significantly faster than a few samplings of digital prototypes for initial screenings.

5.5. Digital Prototype Visualization Verification

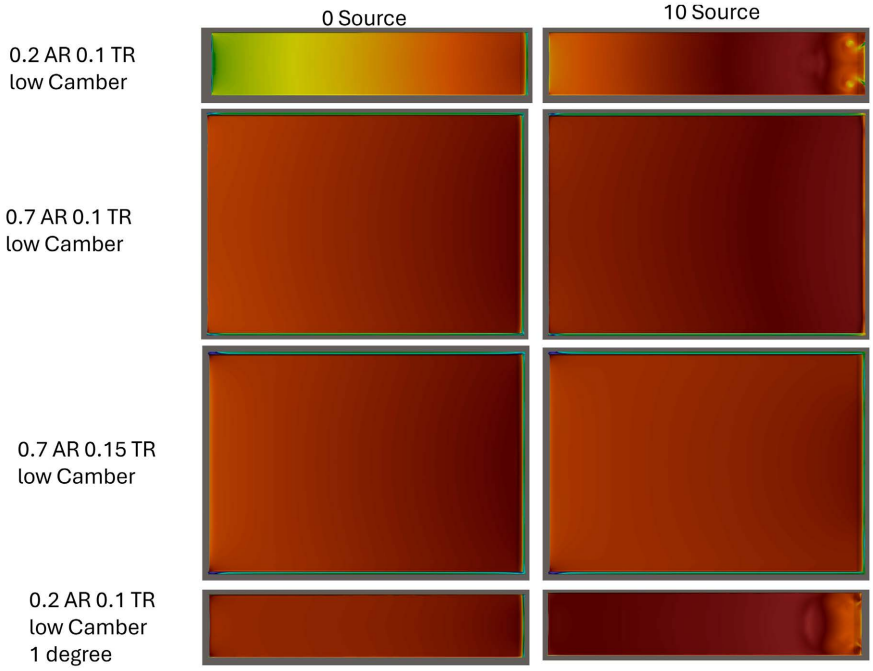

Figure 19. Lower surface pressure contours for sample digital prototypes.

The pressure contour of the lower cavity is especially effective for identifying the problem of lateral dissipation of lift pressures under the fences and methods to mitigate those losses with lower surface pitch and higher aspect ratios as illustrated by Figure 19. At AR = 0.2 with a flat horizontal lower surface, pressure expands from the rear forward with a substantial loss of lift pressures at the forward section of the cavity. An increase in aspect ratio to 0.7 reduces the perimeter

of lift pressure dissipation relative to the area of higher pressure and leads to substantial preservation of lift pressures throughout the lower cavity. Increasing the thickness ratio from 0.1 to 0.15 reduces the robustness of the trailing stagnation region and slightly lowers pressures in the cavity. The use of a 1° pitch on the lower surface generates higher pressures throughout the lower cavity to offset the lateral dissipation throughout the lower cavity.

5.6. Source Power Discussions

Another result of the additional wing section studies resulted from changing the source height to 25% of the values used in the initial studies. The data identify that a shorter Source height is more efficient; however, there is uncertainty about how to interpret higher Source settings in OpenFOAM software. The importance is operation at the optimal condition. Interpretation of the Source setting requires conversions related to Source size, and potentially other currently unquantified values.

Discussion of the direct meaning of the Source setting is avoided through a focus on k, L/D, and drag coefficients with power and energy discussed indirectly in terms of lost work as related to the kinematic turbulence (k). The important findings related to Source power are that the Source power is at an optimal value or at a value resulting in other phenomena such as: a) a failure to overcome boundary layer separation, b) generation or absence of lift-induced drag at the Source intake, and c) generation or absence of jetwash turbulence. All sources outside of the experiments comparing the height of the Source use the same height and chord length dimensions for their sources and span the entire width of the model to avoid differences resulting directly from Source dimensions and implementation.

5.7. Interpretations of Reduced Lost Work

The results identify how a trailing-section upper-surface ducted fan results in lower turbulence and lower lost work associated with the turbulence. This is consistent in 3D simulations, following trends in 2D studies.

The increasing L/D efficiency with onset of sources is consistent from 2D to 3D studies. High L/D leads to significant decreases in energy consumption since rolling losses from wheel suspension may be displaced by aerodynamic suspension. Furthermore, the drag associated with providing aerodynamic lift decreases as L/D efficiency increases.

The 2D simulations identify the pressure drag consistently decreases with the onset of sources, corresponding to the elimination of boundary layer separation. The 3D simulations only show decreasing pressure drag with increasing Source settings for the combinations which achieve the highest L/D efficiency. These trends identify that the ultimate improved performance of GEFT designs reside in the use of more-complex Source configurations and variations of airfoil cross sections to better-mitigate boundary layer separation.

Complementary studies identify that the substantial reductions in energy consumption of already-streamlined vehicles are from the elimination of rolling losses, which provides up to a 50% reduction in energy consumption [39]. About a 50% additional reduction, 75% total, is readily possible by reducing drag.

The following is a suggested ranking of lost work from highest to lowest for GEFT:

1) Turbulence formation (prominent in 2D).

2) Viscous losses (2nd most prominent in 2D).

3) Lateral dissipation from upper surface (3D, prominent).

4) Lateral pressure dissipation losses under fences (3D, key optimization variable).

For free flight aircraft, additional mechanisms of lost work include the increased lateral dissipation of lift pressures from lower surfaces and the downward dissipation of lift pressure forces.

This work benefited from two approaches: a) 3D studies following the understanding gained from 2D studies and b) an accurate fundamental explanation of how air flow generates lift and drag forces. The results are GEFT digital prototype performances with substantial reductions in energy consumption at cruising conditions.

5.8. Excessively High L/D Efficiencies

While decoupling the thrust from the Source from L/D efficiencies is beyond the scope of this work; enough information has been collected to make informed judgements on the meaning of the high L/D, including:

1) L/D increases from boundary layer separation mitigation are achievable and represent a significant leverage of the air flow and pressures generated by the Source; that leverage starts at more than 10:1 energy improvement as the Source setting increase from zero [40].

2) L/D increases up to 80% of the minimum in k represent continued synergy of the trailing-section upper-surface Source on the pressure and velocity contours around the vehicle; the L/D increases are achievable when the leverage of the Source thrust converges from >10:1 at low Source setting to 1:1 in the limit of high Source settings.

3) The pressure buildup from the trailing stagnation region at the lower section of the taper is Source thrust that has undergone the transition from kinetic energy over the mid-section of the taper to pressure at the trailing stagnation region. At source settings greater than the setting corresponding to a minimum in k, the manifestation of higher pressure at the stagnation region unrealistically decreases pressure drag and increases L/D.

4) The generation of jet wash from the trailing taper surface is evidence of inflated L/D values due to pressure acting on rear surfaces. However, before the generation of jetwash, substantial reductions in drag can occur due to mitigation of boundary layer separation and improved streamlining. While the L/D values

may be mildly inflated in this realm of operation, the increased L/D values are indicative of realizable increases in flight efficiency.

Based on these judgments, the representative L/D efficiency is the L/D corresponding to the minimum in k. For purposes of higher consistence, the L/D at an 80% decrease in k toward k-minimum may be used for wing sections. Due to differences in turbulence resulting from lateral dissipation of forces in digital prototypes, L/D at source powers within the order of magnitude of k-min may potentially be considered for digital prototypes.

Substantially inflated values of L/D occur at Source settings greater than that corresponding to a minimum in k. For the results of this paper values of L/D most meaningfully indicate increases in flight efficiency at Source values below approximately 15 for 2D simulations.

Previous results have shown that L/D efficiencies for the GEFT digital prototype design in excess of 50 are possible without power to the Source, with thickness ratios near 0.05 [41]. In this optimal configuration, the pressures at the frontal and rear profiles substantially cancel.

Concurrent work has identified four unique sources of resistance reduction from GEFT: a) mitigation of boundary layer separation with decrease in pressure drag, b) mitigation of rolling resistance by displacing wheel suspension with aerodynamic suspension, c) reduction of the impact of the lead stagnation region, and d) contiguous streamlining of the vehicle's lower surface [39].

The leading edge-stagnation region is an important singularity that initiates the transformation of flow into lift pressures. When boundary layer separation (BLS) occurs over the trailing taper, higher pressures on the front section and lower pressures on the rear section lead to substantial pressure drag. As BLS is mitigated, the frontal and rear pressures become substantially equal and opposite, such that pressures acting on the taper are equal and opposite pressure acting on the front. In the most favorable designs, the leading stagnation region is approximately centered in front of the leading edge where at least part of the pressure countering the trailing taper by the leading stagnation region originates from the cavity.

Some of the counter pressure from the cavity originates from the viscous flow next to the lower surface. Since the viscous resistance is inevitable, it is an ideal source of counter pressure against the leading stagnation region. At optimal conditions, pressure drag approaches viscous drag such that the viscous drag in the cavity approaches half the total drag resistance since pressure drag can be majorly reduced through induced thrust. Consequently, use of the cavity viscous drag to counter the leading stagnation region can lead to a 25% reduction in drag. As the thickness ratio increases, pressure drag increases disproportionately more than viscous drag. As pressure drag decreases below viscous drag there are diminishing returns for L/D efficiency which is inversely proportional to total drag of which viscous drag becomes most prominent.

The interpretation and optimization of GEFT designs is complicated by the manner in which the dynamics of the ducted fan are coupled with the vehicle aer-

odynamics. Anomalies emerge such as L/D > 50, which can persist for 3D digital prototypes. A hypothesis emerges consisting of the following sequence of development as the power of the ducted fan is increased:

1. At zero Source setting, and for the designs of primary interest, boundary layer separation occurs over GEFT's trailing taper.

2. As the Source initializes, the Source exhibits increased effectiveness in mitigating boundary layer separation. Increases in L/D efficiency are mostly fundamental, based on changes in the pressure contour around the vehicle. During this phase of Source power initialization turbulence decreases.

3. Eventually, the boundary layer is substantially displaced with laminar flow over the trailing taper associated with the formation of the trailing-edge stagnation region. This condition corresponds with a minimum in turbulence.

4. As the trailing-edge stagnation region increases, it effectively displaces Source thrust forces from the Source to the lower section of the trailing taper which leads to artificially decreased drag and artificially higher L/D efficiencies. Further increased Source settings lead to increasing turbulence from additional jetwash.

The hypothesis components 1 - 4 identify phenomenon primarily associated with decreasing the pressure drag, correspondingly increasing L/D. Additional components of the hypothesis include interactions from the cavity:

5. A robust lower cavity lift pressure has contributions from multiple phenomena, including:

a) A trailing-edge stagnation region extending from the trailing flap edge to the ground, which can expand forward into the cavity with implicit mitigation of higher pressures in from the cavity under the flap.

b) A minimum fence-ground clearance, based on terrain and the ability to prevent the fence from impacting the ground minimizes dissipation of higher-pressure cavity lift forces under the fences. At very low fence clearances, viscous drag between the bottom of the fence and the ground increases and causes inefficiencies.

c) A slightly positive lower surface pitch which can generate higher pressures at the same rate pressure is dissipated; this inherently minimizes lost work by providing an overall minimum average driving force for dissipation under the fence.

6. When the higher pressures reach the leading edge within these constraints, at least part of the higher-pressure leading-edge stagnation point is countered by viscous force generated pressures in the cavity leading to a lower pressure drag from the leading-edge stagnation region than is possible without this approach.

Hypothesis components 5a-5b lead to high cavity-based lift forces which approach a contribution of 1.0 to the vehicle's overall lift coefficient.

5.9. A Working Hypothesis Overview

The Hypothesis components 4 and 6 provide further clarification in a parallel

work that includes data on pressure contours at trailing-edge and trailing-edge stagnation regions [39]. Pressure contours from low Source settings are consistent with non-optimal aerodynamics; both boundary-layer separation and loss of higher cavity pressures under the trailing flap are present. Pressure profiles where a trailing stagnation region begins to appear are consistent with hypothesis component 4 where thrust forces are transferred to the back side of the flap and L/D values are distorted on the high side. The 2D L/D values in Table 2 are considered as at optimal Source settings where the L/D are representative albeit high due to the 2D CFD assumptions. Table 2 data have not been evaluated to identify optimal Source values; a decision that was made in part to further optimization on the 3D prototypes to better reduce lost work.

The current work includes using a minimum in turbulence from the CFD mesh to identify an optimal Source setting based on the design and free stream velocity. The assumption of these studies is that minimum kinematic turbulence approximates a minimum in lost work and further corresponds to a near-optimum Source setting. The value in these studies is that a single optimal L/D can be assigned to a given wing section design for comparison to other wing sections.

5.10. Performance Objectives

The A performance objective is to achieve an L/D efficiency of greater than 20 near a minimum in turbulence which is typically associated with a lift coefficient greater than 1.0, an absence of boundary layer separation, and minimal jetwash. To avoid jetwash, additional thrust can be provided by wheels. Braking can be provided by a controlled release of lower cavity pressure alongside regenerative braking.

Table 5 converts example vehicle dimensions to AR and TR for comparison to the 3D digital protypes. Problematic parameters such as cabin heights that are too low and high aspect ratios may be compared. Table 6 provides additional degrees of freedom to achieve higher L/D and more-effectively mitigate boundary layer separation.

Table 5. Example relation of vehicle dimensions to AR and TR. Key functionality parameters for relation to GEFT designs are in italics.

Vehicle	Width (m)	Height (m)	Length (m)	AR	TR	Compatibility with GEFT
Semi-Trailer Truck	2.6	2	20	***0.13***	0.1	AR is too low
Short Box Truck	2.6	***1.3***	13	0.2	0.1	Efficient, but low height
Box Truck	2.6	2	13	0.2	***0.15***	TR on the high side
Autonomous Truck (Theoretical)	2.6	1.3	13	0.2	0.1	Great GEFT potential

Continued

Trailer	2	0.6	6	0.33	0.10	Great GEFT potential
Automobile	2	1	6	0.33	***0.33***	TR is too large
Ship (Catamaran)	20	3	20	1.0	0.15	Restricted to wide waterways

Viable vehicle options based on the data of this paper include the autonomous truck and trailer. The autonomous truck does not need a cabin nor trailer at walking height for use with autonomous loading and unloading; it remains compatible with manual operation, allowing loading and unloading at the 1.3 m in height.

The trailer is a particularly favorable option when operated as a tow-assist trailer using solar power and batteries. The lower tow resistance allows smaller vehicles and common automobiles to pull these trailers. Powering the trailer with solar panels, batteries, and regenerative braking both reduces fuel consumption and the load on the lead vehicle [39].

Table 6. Example parameters to further optimize GEFT.

Parameter	Example Conditions
Source Shape	Height impacts performance
Source Location on Trailing Taper	Within upper 10% of vertical expanse
Source Thrust Vector	From 0 to 15 °, horizontal and downward vector
Trailing Taper Shape	Slight convex-upward camber
Step-Change in Pitch at Source	From 0° to 15°
Fence Shapes	Create induce thrust on some of frontal surface and as well as multiple control surfaces along camber length
Fence Height	From 5% to 25% of cabin height
Number of Fence Pairs	One or two pairs with middle pair consisting of a lateral span at least 50% of the vehicle width
Fence Clearance	From 1% to 5% of cabin height, constant throughout
Flap Shape	Contiguous upper surface with taper
Flap Clearance	2X to 4X fence clearances
Average Pitch of Lower Surface	From 0° to 2° nose up
Camber of Lower Surface	0% to 5% concave downward, 0% at front 10% of chord
Front Deflector	Convex upward with a pitch of −45° to −15° at leading edge
Lateral Surface Extensions	From wings to thin camber extension of lifting body

Continued

Slats	Contiguous with front deflector surface and as control surface
Blowers to Cavity	Blowers with discharge to supplement cavity pressure
Transition from Leading Vehicle	Frontal Ducted Fan
Mid-Cavity Flaps	To mediate lift forces and control stability through dividing the cavity into sections
Trailing taper as Chord Fraction	50% to 20% of chord.
Headroom canopy size, shape, and location (midsection variation).	A canopy for headroom of drivers and passengers in an automobile.
Headroom canopy ducted fan size, location, and setting (midsection variation).	Canopies of shape similar to the GEFT airfoil but with the objective of streamlining flow to the trailing taper of the base case GEFT body.
Lateral Variation of Airfoil Cross-Section	Lower height toward sides Includes driver and passenger canopy higher than rest of upper surface
Additional/Distributed Propulsion Sources	Near or on sides in combination with trailing taper shape to further mitigate boundary layer separation

Several of the parameters and ranges of Table 6 are known to improve L/D but were outside the scope of the current study [26]. Past results indicate that a TR = 0.15 at AR = 0.2 can achieve an L/D greater than 20. Table 7 summarizes viable and potential applications of GEFT technology.

Table 7. Viable and likely markets based on digital prototype performance and degrees of freedom.

Market	Viability Comments
Viable Per Digital Prototypes	
Autonomous Truck	Viable due to payload height of 1.3 meter or less for robot loading and unloading of payload.
Tow-Assist Trailers	Viable at low cabin heights consistent with much cargo.
Other Trucks, Railcars, and multimodal vehicles	Viable with optimization of performance parameters to attain TR > 0.15 with anticipated further optimization.
Catamaran Ship (open seas, marine transit, ferries)	Viable based on AR > 0.5 as highly compatible with open waters.
Likely Viable	
Automobile	Anticipated viability with driver canopy extending above the rest of the vehicle surface and with lower surface at average pitch up to 2.5˚.

Continued

Water Sports	Viable based on AR > 0.5 possible with passenger canopy.
Tunnel Transit	In tunnels, the upper surface of the vehicle in combination of with upper surface of the tunnel are able to form a nacelle for the Source which can enable even higher L/D efficiencies with other advantages such as engineered tailwinds and passively reduced pressures [42].
	Partial Benefit
Broadly Applicable	Mitigation of boundary layer separation reduces drag. Partial aerodynamic lift reduces wheel suspension. Lower leading-stagnation region reduces pressure drag through use of lower-surface viscous drag to displace part of forward pressure drag.

Viable applications include trucks and trailers that operate at heights less than 1.5 m as which are compatible with robot loading and unloading from the rear of the payload compartment. Loading from sides at TR < 0.15 is broadly applicable. Catamaran ships and ferries are broadly viable due to AR > 0.5 as ideal for open waters, allowing large vehicle sizes with corresponding increases in cabin heights with highly efficient vehicles possible at AR > 1.

Preliminary studies have verified that a headspace canopy is able to increase the thickness ratio while achieving a range of automobile and bus designs viable at L/D > 20. This is a subject of concurrent studies.

The technology is broadly applicable once substantial reductions in resistance are achieved. The corresponding increases in energy efficiency are possible with a focus on mitigating losses from trailing-section boundary layer separation and reduced pressure drag from the leading stagnation region. Reasonable and effective partial displacement of rolling losses occurs at 10 < L/D < 20 for a broad range of applications. Up to 50% reductions in energy consumption are possible; this compiles to reductions up to 80% when the vast majority of wheel suspension is displaced with aerodynamic suspension.

GEFT have the propensity to provide many operational advantages such as: a) transit speeds on highways and tracks greater than the traction and stress limits of wheel-based vehicles, b) greater efficiency than other wheel-based or free-flight alternatives, c) an evolutionary path of greater potential as seamless multimodal vehicles, and d) applications capable of operation using only direct solar power [39]. **Tables 5-7** provides a summary of applications based on category.

The ability to achieve L/D efficiencies exceeding 20 at widths compatible with highways and reasonable heights provide major advances over current vehicle alternatives. This paper identifies that all but the lowest TR applications are possible through the trailing-section upper-surface ducted fan used in combination with

the trailing taper and lower cavity; the innovation is further defined in a 2024 patent application [43]. The combination of a broad range of more-efficient higher-speed applications enabled by a new aerodynamic explanation approach supported by both molecular and continuum mechanics could meet the definition scientific revolution [44].

GEFT is a premium application to demonstrate the capabilities of CFD, advantages of improved understanding, and optimization algorithms.

5.11. Concerns of 2D Simulations

Two-dimensional simulations fail to account for how optimal lower surface pitches can increase L/D efficiency in 3D and actual vehicles, as illustrated in **Figure 12**. In 2D, the pressure effectively expands from the leading edge rearward while in 3D rearward expansion from the leading stagnation region does not emerge. In 3D, a robust trailing stagnation region expands forward; therefore, lower surface pitch and concavity are able to progressively generate lift from the lower surface. In 2D, a lower-surface pitch primarily manifests as lift-induced drag which diminishes L/D.

The degrees of freedom for especially high impact unique to 3D simulations are:

1) Lower surface pitch, including slight concavity.

2) Spanwise variation of airfoil including use of a canopy.

3) Spanwise variation of ducted fan shape and location.

Variations in fences, flaps, and extendable wings.

5.12. Alternative Results-Oriented Objective Function

The objective function for this study was vehicle volume-specific turbulence using the k/TR metric. For loads of minimum volume, such as video and electronics, vehicle height does not necessarily correlate with vehicle and payload performance. Two alternative objective functions would have common utility:

Minimum Height based upon application since L/D tends to increase with decreasing wing section thickness. Typical minimum heights might be 1 m for an automobile and 2 m for a railcar or bus. Vehicle length can be varied depending on these constraints.

Toward Autonomous Vehicles and Payload Handling. As androids and autonomous vehicles displace trucking based on semi-truck trailers, lower height trucks and higher aspect ratio trucks become viable; the freight cabins do not need to accommodate walking or tow motors. In these applications further reductions in energy consumption are available. L/D values near 40 are attainable.

Minimum Ground Clearance correlates with surface deviation tolerances. For example, operation over choppy waters, as with ships and boats, flight would be limited to a maximum expected wave height. Ground clearance can be increased by increasing the height and size of the vehicle. Railroads may provide the narrowest clearances.

6. Conclusions

A rigorous energy efficiency analysis of a new ground-effect flight transit vehicle (GEFT) is complicated by the manner in which the aerodynamics of the ducted fan are coupled with GEFT's lifting-body surfaces. An analysis of lost work based on kinematic turbulent energy was able to overcome these complications by correlating turbulence with ducted fan power setting to identify a kinematic turbulence minimum. The minima correspond to the end of boundary layer separation and onset of jetwash. This approach allows different vehicle designs to be compared at optimal operating conditions to identify better vehicle designs.

An objective function of reducing turbulence per volume of payload leads to optimal TR between 0.1 and 0.2. If the objective is a greater emphasis on weight rather than volume, lower TR designs emerge as optimal. Vehicles designed under the constraint of a maximum width of 2.6 m have insufficient headroom at typical lengths, requiring function specific optimization to extend the applications to most wheeled vehicle transit applications.

Over twenty design degrees of freedom and computationally intensive CFD simulations mandate efficient approaches to design optimization. The approach of this paper uses initial 2D studies with interpretations of data to reduce design options prior to more intensive 3D CFD studies. Additional parameters needed for 3D versus 2D CFD include fence clearance and vehicle aspect ratio, both of which have a high impact on performance.

GEFT technology is in a phase of rapid evolution. Concurrent efforts on physical prototype fabrication and evaluation would lead to prototypes that are obsolete before completion of the physical prototype analysis. Consequently, the R&D path implicitly tests the capabilities of digital prototypes and CFD simulations. Relating digital prototype performances to a new airfoil science based on Three Principles, grounded in physics, is a level of validation for these studies, in lieu of immediate experimental validation. Benefits of this approach are the rapidly advancing designs and understanding.

GEFT science and technology have potentially profound impacts on transportation and society. GEFT's unique design generates aerodynamic lift, reduces associated wheel/mechanical resistances, and concurrently reduces aerodynamic drag from: a) boundary layer separation, b) the leading stagnation region pressure, and c) the vehicle's lower surface. While high-speed applications where wheeled suspension is displaced with aerodynamic lift realize the greatest reductions in energy consumption, the novel approaches to reducing drag are widely applicable to many wheeled vehicles and trailers.

Conflicts of Interest

The authors declare no conflicts of interest regarding the publication of this paper.

References

[1] Suppes, A., Suppes, G., Lubguban, A. and Al-Moameri, H. (2025) An Airfoil Science

Including Causality. *Sustainable Engineering and Technological Sciences*, **1**, 12-31. https://doi.org/10.70516/j215nh63

[2] Tse, T.S. and Hall, C.A. (2020) Flow Field and Power Balance of a Distributed Aft-Fuselage Boundary Layer Ingesting Aircraft. *AIAA Propulsion and Energy* 2020 *Forum*, New Orleans, 24-28 August 2020. https://doi.org/10.2514/6.2020-3779

[3] Fard, M.T., He, J., Huang, H. and Cao, Y. (2022) Aircraft Distributed Electric Propulsion Technologies—A Review. *IEEE Transactions on Transportation Electrification*, **8**, 4067-4090. https://doi.org/10.1109/tte.2022.3197332

[4] Erhard, R.M., Clarke, M.A. and Alonso, J.J. (2021) A Low-Cost Aero-Propulsive Analysis of Distributed Electric Propulsion Aircraft. *AIAA Scitech* 2021 *Forum*, Nashville, 19-21 January 2021. https://doi.org/10.2514/6.2021-1200

[5] Kim, H.D., Perry, A.T. and Ansell, P.J. (2018) A Review of Distributed Electric Propulsion Concepts for Air Vehicle Technology. 2018 *AIAA/IEEE Electric Aircraft Technologies Symposium*, Cincinnati, 9-11 July 2018, 1-21. https://doi.org/10.2514/6.2018-4998

[6] Machado, L., Chau, T. and Kenway, G.K. (2023) Preliminary Assessment of a Distributed Electric Propulsion System for the SUSAN Electrofan. National Harbor.

[7] Rothhaar, P.M., Murphy, P.C., Bacon, B.J., Gregory, I.M., Grauer, J.A., Busan, R.C., *et al.* (2014) NASA Langley Distributed Propulsion VTOL Tiltwing Aircraft Testing, Modeling, Simulation, Control, and Flight Test Development. 14*th AIAA Aviation Technology, Integration, and Operations Conference*, Atlanta, 16-20 June 2014. https://doi.org/10.2514/6.2014-2999

[8] Serrano, J.R., Tiseira, A.O., García-Cuevas, L.M. and Varela, P. (2021) Computational Study of the Propeller Position Effects in Wing-Mounted, Distributed Electric Propulsion with Boundary Layer Ingestion in a 25 kg Remotely Piloted Aircraft. *Drones*, **5**, Article 56. https://doi.org/10.3390/drones5030056

[9] Gohardani, A.S., Doulgeris, G. and Singh, R. (2011) Challenges of Future Aircraft Propulsion: A Review of Distributed Propulsion Technology and Its Potential Application for the All Electric Commercial Aircraft. *Progress in Aerospace Sciences*, **47**, 369-391. https://doi.org/10.1016/j.paerosci.2010.09.001

[10] Ma, Y., Zhang, W. and Elham, A. (2022) Multidisciplinary Design Optimization of Twin-Fuselage Aircraft with Boundary-Layer-Ingesting Distributed Propulsion. *Journal of Aircraft*, **59**, 1588-1602. https://doi.org/10.2514/1.c036559

[11] Russo, O., Aprovitola, A., de Rosa, D., Pezzella, G. and Viviani, A. (2022) Computational Fluid Dynamics Analyses of a Wing with Distributed Electric Propulsion. *Aerospace*, **10**, Article 64. https://doi.org/10.3390/aerospace10010064

[12] Borer, N.K., Derlaga, J.M., Deere, K.A., Carter, M.B., Viken, S., Patterson, M.D., *et al.* (2017) Comparison of Aero-Propulsive Performance Predictions for Distributed Propulsion Configurations. 55*th AIAA Aerospace Sciences Meeting*, Grapevine, 9-13 January 2017. https://doi.org/10.2514/6.2017-0209

[13] Felder, J., Brown, G. and Dae Kim, H. (2011) Turboelectric Distributed Propulsion in a Hybrid Wing Body Aircraft.

[14] Finger, D., Braun, C. and Bil, C. (2017) A Review of Configuration Design for Distributed Propulsion Transitioning VTOL Aircraft. 2017 *Asia-Pacific International Symposium on Aerospace Technology*, Seoul, 16-18 October 2017, 1-15.

[15] Jones, C.E., Norman, P.J., Galloway, S.J., Armstrong, M.J. and Bollman, A.M. (2016) Comparison of Candidate Architectures for Future Distributed Propulsion Aircraft. *IEEE Transactions on Applied Superconductivity*, **26**, 1-9. https://doi.org/10.1109/tasc.2016.2530696

[16] Leifsson, L., Ko, A., Mason, W., Schetz, J., Haftka, R. and Grossman, B. (2011) Multidisciplinary Design Optimization for a Blended Wing Body Transport Aircraft with Distributed Propulsion.

[17] Zhang, X., Zhang, W., Li, W., Zhang, X. and Lei, T. (2023) Experimental Research on Aero-Propulsion Coupling Characteristics of a Distributed Electric Propulsion Aircraft. *Chinese Journal of Aeronautics*, **36**, 201-212. https://doi.org/10.1016/j.cja.2022.07.024

[18] Lee, T. and Lin, G. (2022) Review of Experimental Investigations of Wings in Ground Effect at Low Reynolds Numbers. *Frontiers in Aerospace Engineering*, **1**, Article 975158. https://doi.org/10.3389/fpace.2022.975158

[19] Shams Taleghani, A., Ghajar, A. and Masdari, M. (2020) Experimental Study of Ground Effect on Horizontal Tail Effectiveness of a Conceptual Advanced Jet Trainer. *Journal of Aerospace Engineering*, **33**, No. 4. https://doi.org/10.1061/(asce)as.1943-5525.0001140

[20] Deviparameswari, K., Meenakshi, S., Akshay Kumar, N., Vigneshwaran, R., *et al.* (2021) The Effects of Ground Clearance and Boundary Layer Blockage Factor on the Aerodynamics Performance of the Hyperloop Pod and Transonic Ground-Effect Aircraft. 2021 *AIAA Aviation Forum*, 2-6 August 2021. https://doi.org/10.2514/6.2021-2586

[21] Qu, Q., Wang, W., Liu, P. and Agarwal, R.K. (2015) Airfoil Aerodynamics in Ground Effect for Wide Range of Angles of Attack. *AIAA Journal*, **53**, 1048-1061. https://doi.org/10.2514/1.j053366

[22] Lee, S. and Lee, J. (2012) Optimization of Three-Dimensional Wings in Ground Effect Using Multiobjective Genetic Algorithm. *Journal of Aircraft*, **48**, 1633-1645. https://doi.org/10.2514/1.c031328

[23] Lee, S. and Lee, J. (2013) Aerodynamic Analysis and Multi-Objective Optimization of Wings in Ground Effect. *Ocean Engineering*, **68**, 1-13. https://doi.org/10.1016/j.oceaneng.2013.04.018

[24] Hu, H., Zhang, G., Li, D., Zhang, Z., Sun, T. and Zong, Z. (2022) Shape Optimization of Airfoil in Ground Effect Based on Free-Form Deformation Utilizing Sensitivity Analysis and Surrogate Model of Artificial Neural Network. *Ocean Engineering*, **257**, Article 111514. https://doi.org/10.1016/j.oceaneng.2022.111514

[25] Suppes, A.B. and Suppes, G.J. (2025) Lost Work Insights into Ground-Effect Aircraft Efficiency. Submitted for Review: ASME.

[26] Suppes, A. and Suppes, G. (2025) Review and Evolution of Ground Effect Flight Transit Vehicles (GEFT). Cambridge Open Engage.

[27] Suppes, A.B. and Suppes, G.J. (2025) Aerodynamics: A Different Perspective with Profound Implications. *Frontiers in Mechanical Engineering*, **11**, Article 1616607. https://doi.org/10.3389/fmech.2025.1616607

[28] Klose, B., Spedding, G. and Jacobs, G. (2021) Direct Numerical Simulation of Cambered Airfoil Aerodynamics at Re = 20,000. https://doi.org/10.48550/arXiv.2108.04910

[29] Michna, J. and Rogowski, K. (2022) Numerical Study of the Effect of the Reynolds Number and the Turbulence Intensity on the Performance of the NACA 0018 Airfoil at the Low Reynolds Number Regime. *Processes*, **10**, Article 1004. https://doi.org/10.3390/pr10051004

[30] Lee, D., Nonomura, T., Oyama, A. and Fujii, K. (2015) Comparison of Numerical Methods Evaluating Airfoil Aerodynamic Characteristics at Low Reynolds Number. *Journal of Aircraft*, **52**, 296-306. https://doi.org/10.2514/1.c032721

[31] Bulat, P., Chernyshov, P., Prodan, N. and Volkov, K. (2024) Control of Aerodynamic Characteristics of Thick Airfoils at Low Reynolds Numbers Using Methods of Boundary Layer Control. *Fluids*, **9**, Article 26. https://doi.org/10.3390/fluids9010026

[32] Suppes, A., Suppes, G. and Al-Moameri, H. (2025) Overcoming Boundary-Layer Separation with Distributed Propulsion. *Sustainable Engineering and Technological Sciences*, **1**, 71-89. https://doi.org/10.70516/7a9e2y30

[33] Han, S., Wang, Y., Zhang, M., Chen, J. and Zhang, J. (2025) An Adaptive Drag Reduction Method for High-Speed Trains across Variable Reynolds Numbers. *Physics of Fluids*, **37**, Article 085208. https://doi.org/10.1063/5.0281229

[34] Machaj, K., Malecha, Z. and Wrzecioniarz, P. (2020) Numerical and Analytical Study of a Battery Powered Vehicle Moving in a Vacuum Tunnel. *World Electric Vehicle Journal*, **11**, Article 26. https://doi.org/10.3390/wevj11010026

[35] Wang, A. and Lai, H. (2024) Control of Separated Flow at Low Reynolds Number around NACA0012 Airfoil by Boundary Layer Suction. *Journal of Physics: Conference Series*, **2707**, Article 012122. https://doi.org/10.1088/1742-6596/2707/1/012122

[36] Williams, O., Samuell, M., Sarwas, E.S., Robbins, M. and Ferrante, A. (2020) Experimental Study of a CFD Validation Test Case for Turbulent Separated Flows. *AIAA Scitech* 2020 *Forum*, Hyatt Regency Orlando, 6-10 January 2020. https://doi.org/10.2514/6.2020-0092

[37] Traub, L.W. and Coffman, C. (2019) Efficient Low-Reynolds-Number Airfoils. *Journal of Aircraft*, **56**, 1987-2003. https://doi.org/10.2514/1.c035515

[38] Winslow, J., Otsuka, H., Govindarajan, B. and Chopra, I. (2017) Basic Understanding of Airfoil Characteristics at Low Reynolds Numbers (104-105). *Journal of Aircraft*, **55**, 1050-1061. https://doi.org/10.2514/1.c034415

[39] Suppes, A. and Suppes, G. (2025) Expanding Electric and Vehicle-Based Solar Transit Options with Breakthrough Vehicular Efficiencies. *World Electric Vehicle Journal*, **16**, Article 628.

[40] Suppes, G.J. and Suppes, A.B. (2023) Thermodynamic Analysis of Distributed Propulsion. Research Square. https://doi.org/10.21203/rs.3.rs-4670270/v1

[41] Suppes, G. and Suppes, A. (2024) Ground Effect Flight Transit (GEFT)—Approaches to Design. Cambridge University Press. https://www.cambridge.org/engage/coe/article-details/66b2340b01103d79c5e7ab23

[42] Suppes, A.B. and J. Suppes, G. (2025) Low-Risk High-Reward Transition to Low Pressure Tunnel Transit. *Engineering and Technology Journal*, **10**, 4994-5004. https://doi.org/10.47191/etj/v10i05.28

[43] Suppes, A. and Suppes, G. (2024) Ground Effect Machine System. https://patentscope.wipo.int/search/en/detail.jsf?docId=WO2025147444

[44] Kuhn, T.S. (1970) The Structure of Scientific Revolutions. University of Chicago Press.